Assessment of hydrogen embrittlement behavior in Al-Zn-Mg alloy through multi-modal 3D image-based simulation

Fujihara, Hiro
Department of Mechanical Engineering, Kyushu University

Toda, Hiroyuki
Department of Mechanical Engineering, Kyushu University

Ebihara, Ken-ichi
Center for Computational Science & e-Systems, Japan Atomic Energy Agency

Kobayashi, Masakazu
Department of Mechanical Engineering, Toyohashi University of Technology

他

https://hdl.handle.net/2324/7234049

出版情報：International Journal of Plasticity. 174, pp.103897-, 2024-03. Elsevier
バージョン：

International Journal of Plasticity 174 (2024) 103897

Contents lists available at ScienceDirect

International Journal of Plasticity

journal homepage: www.elsevier.com/locate/ijplas

Assessment of hydrogen embrittlement behavior in Al-Zn-Mg alloy through multi-modal 3D image-based simulation

Hiro Fujihara [a,*], Hiroyuki Toda [a], Ken-ichi Ebihara [b], Masakazu Kobayashi [c], Tsuyoshi Mayama [d], Kyosuke Hirayama [e], Kazuyuki Shimizu [f], Akihisa Takeuchi [g], Masayuki Uesugi [g]

[a] *Department of Mechanical Engineering, Kyushu University, 744 Motooka, Nishi-ku, Fukuoka 819-0395, Japan*
[b] *Center for Computational Science & e-Systems, Japan Atomic Energy Agency, Ibaraki 319-1195, Japan*
[c] *Department of Mechanical Engineering, Toyohashi University of Technology, Aichi 441-8580, Japan*
[d] *Department of Materials Science and Engineering, Kumamoto University, Kumamoto 860-8555, Japan*
[e] *Department of Materials Science and Engineering, Kyoto University, Kyoto 606-8501, Japan*
[f] *Department of Physical Science and Materials Engineering, Iwate University, Iwate 020-0061, Japan*
[g] *Japan Synchrotron Radiation Research Institute, Hyogo 679-5198, Japan*

ARTICLE INFO

Keywords:
Hydrogen embrittlement
Al-Zn-Mg alloys
X-ray tomography
Diffraction contrast tomography
3D image-based simulation
Crystal plasticity finite element method
Hydrogen diffusion

ABSTRACT

Hydrogen can strongly embrittle aluminum alloys by accumulating at precipitate interface and triggering transgranular cracking, due to stress-driven hydrogen diffusion towards crack tip and grain boundaries. However, although mechanical features near crack tip and grain boundaries, and hydrogen diffusion/trapping processes have been extensively studied separately, very few quantitative information regarding the local interactions between hydrogen distribution and stress fields with full spatial complexity has been revealed. The present study attempts to fill this gap, by using a multi-modal three-dimensional image-based simulation that combines a crystal plasticity finite element method with hydrogen diffusion analysis, to fully capture the actual stress distribution and its effect on hydrogen distribution, and more importantly on cracking probability, near a real propagating hydrogen-induced crack. Stress-diffusion-trapping coupled simulations indicate the intergranular crack transitioned to a quasi-cleavage crack in the region where the interfacial cohesive energy of semi-coherent interface of the $MgZn_2$ precipitate was reduced by hydrogen accumulation near the crack tip. The multi-modal three-dimensional image-based simulation used in the present study successfully bridged nanoscopic debonding and macroscopic hydrogen embrittlement fracture behavior.

1. Introduction

The presence of hydrogen in metallic materials degrades their mechanical properties, such as ductility, in a phenomenon known as hydrogen embrittlement (HE) (Lynch, 2012; Robertson et al., 2015). Birnbaum et al. (1994) numerically investigated the interaction between dislocations and hydrogen and proposed the hydrogen-enhanced localized plasticity (HELP) mechanism, in which hydrogen trapped at dislocations causes reduced interactions among dislocations on the same slip plane. Tabata et al. (1983, 1984)

---

[*] Corresponding author.
E-mail address: fujihara@mech.kyushu-u.ac.jp (H. Fujihara).

https://doi.org/10.1016/j.ijplas.2024.103897
Received 21 October 2023; Received in revised form 23 January 2024;

experimentally showed via transmission electron microscopy (TEM) that dislocation mobility increases with increasing hydrogen pressure. In contrast, there are reports indicating that hydrogen pins dislocations (Deng and Barnoush, 2018; Xie et al., 2016; Zhu et al., 2017), and that it acts as a solution atom in solute-hardening behavior (e.g., like carbon in steel). In the hydrogen-enhanced decohesion (HEDE) mechanism, hydrogen trapped at boundaries (e.g., grain boundaries) reduces the cohesive strength and accelerates crack initiation and propagation (Oriani and Josephic, 1974; Troiano, 2016). Oriani et al. (1974), who calculated the reduction in cohesive strength through hydrogen accumulation in 4340 steel, reported an approximately 40 % decrease in cohesive strength when the hydrogen concentration was 10^4 times the equilibrium concentration. Based on HEDE mechanism, some reports indicated that accumulated hydrogen at grain boundaries and/or twin boundaries promotes intergranular fracture (Elkot et al., 2022; Liang et al., 2021; Safyari et al., 2021). Nagumo et al. (2004) proposed another HE mechanism, the hydrogen-enhanced strain-induced vacancy (HESIV) mechanism, in which hydrogen can accelerate the accumulation of vacancies and the formation of nanovoids. Associated studies reported that vacancy act as the primary factor for hydrogen-induced fracture rather than hydrogen, and they concluded that this behavior agrees with the HE with HESIV model (Nagumo and Takai, 2019; Takai et al., 2008).

Mixture mechanisms have also been proposed (Djukic et al., 2019, 2015; Neeraj et al., 2012; Wasim et al., 2021). Using high-resolution surface sensitive scanning electron microscopy, Neeraj et al. (2012) observed fracture surface features. Then, they proposed that quasi-cleavage fracture, a hydrogen embrittlement fracture mode, occurred due to plasticity-generated and hydrogen-stabilized vacancy damage accumulation and nanovoid coalescence (i.e., HELP + HESIV) in ferritic steel. Djukic et al. (2015, 2019), Wasim et al. (2021) proposed the HELP + HEDE model. These authors indicated that there was a mixture of micro-void coalescence and transgranular brittle and intergranular fractures on the fracture surface of ferritic-pearlitic steel, and they concluded that these fracture modes were attributed to HELP and HEDE in the grain interior and HEDE in the grain boundary, respectively. Then, they proposed that the fracture mode could dominate with both HEDE and HELP dominating at mid-to-high hydrogen concentrations. This mixed model can also be accepted for aluminum alloys (Moshtaghi et al., 2021). From these proposed nanoscopic HE mechanisms and/or these mixed mechanisms, the interaction between hydrogen and nano-defect should promote macroscopic HE behavior.

Ismer et al. (2009), Yamaguchi et al. (2019, 2021), who investigated the hydrogen trapping behavior at trap sites in an aluminum alloy using first-principles calculations, reported that vacancies, dislocations and grain boundaries have lower hydrogen trapping energies than other trap sites for which the trap energy was previously reported (e.g., precipitates, intermetallic compound particles, and micropores Shimizu et al., 2024; Tsuru et al., 2018; Yamaguchi et al., 2020, 2018). Su et al. (2019), Shimizu et al. (2019), who analyzed hydrogen partitioning behavior using these trap energies, reported that the hydrogen concentration at these trap site was less than 0.001 % of the total hydrogen concentration in Al-Zn-Mg alloys. Therefore, the abovementioned mechanisms, which involve interactions between hydrogen and dislocations, grain boundaries, and vacancies, do not appear to be significant contributing factors to HE in Al-Zn-Mg alloys.

Recently, using first-principles calculations, Tsuru et al. (2020) reported that the interface between $MgZn_2$ precipitates and aluminum spontaneously debonds without stress when the hydrogen concentration at the interface reaches approximately 10^{26} atoms H/m^3 (i.e., 61 mass ppm), and traces of the debonding behavior of the precipitate interface were observed on the quasi-cleavage fracture surface. Then, they proposed this as a new mechanism of quasi-cleavage fracture in Al-Zn-Mg alloys (Tsuru et al., 2020); additionally, they reported that the $MgZn_2$ precipitate interface has a higher hydrogen trap energy than the other trap sites, and more than 90 % of the total hydrogen was trapped at this interface (Shimizu et al., 2024; Tsuru et al., 2018). During deformation, most of the accumulated hydrogen could be locally partitioned to the precipitate interface and reach the critical hydrogen concentration for hydrogen-induced debonding (i.e., 10^{26} atoms H/m^3) (Tsuru et al., 2020, 2018). This hydrogen accumulation leads to nano-crack initiation at the precipitate interface, and eventually, macroscopic HE fracture could occur due to the coalescence of these nano-cracks. In addition, the present authors experimentally observed HE crack propagation behavior in Al-Zn-Mg alloys through *in-situ* tensile testing with frequent interruptions and found that the HE crack propagation rate increased with increasing interruption time (Su et al., 2018). This trend indicates that crack propagation is due to local hydrogen accumulation caused by hydrogen diffusion under stress. Therefore, the local hydrogen accumulation behavior under stress must be investigated to determine whether there is a correlation between nanoscopic hydrogen-induced debonding and macroscopic HE fracture behavior. However, the author's previous studies (Shimizu et al., 2020; Su et al., 2019; Wang et al., 2022) could not quantitatively associate macroscopic HE fractures with nanoscopic debonding behavior due to local hydrogen accumulation because we could not include an analysis that takes stress-induced hydrogen accumulation behavior into account.

To evaluate dynamic and quantitative hydrogen accumulation behavior, analysis of the hydrostatic stress distribution, which acts as a driving force for hydrogen diffusion, is crucial (Isfandbod and Martínez-Pañeda, 2021; Li et al., 1966). There have been numerous attempts to quantify hydrogen diffusion behavior under stress using the finite element method (FEM) (Barrera et al., 2016; Dadfarnia et al., 2015; Fernández-Sousa et al., 2022). However, these continuum model-based analyses reveal that hydrogen diffusion behavior depends on macroscopic material properties but cannot consider microstructural effects. Instead, an 'effective diffusion coefficient' concept is utilized in such simulations (Yuan et al., 2023). In polycrystalline materials, stress and strain locally accumulate around specific grain boundaries due to interactions among neighboring grains (Guo et al., 2015; Hayashi et al., 2019; Toda et al., 2016; Tondro and Abdolvand, 2022; Yuan et al., 2020). The crystal plasticity finite element method (CPFEM), a numerical simulation that can evaluate the slip deformation behavior of individual grains, is known as an effective method for evaluating the local stress distribution in polycrystalline materials (Miresmaeili et al., 2010; Raabe and Roters, 2004). Additionally, by combining hydrogen diffusion analysis with the CPFEM, the temporal evolution behavior of local hydrogen accumulation can be analyzed in polycrystalline materials (Miresmaeili et al., 2010; Tondro and Abdolvand, 2022). For example, Miresmaeili et al. (2010), who simulated the stress, strain, and hydrogen distribution in polycrystalline steel with artificial microstructures by employing CPFEM and hydrogen diffusion analysis, reported that the stress and hydrogen locally concentrated around a specific grain boundary. The CPFEM may be considered an effective method for estimating the local stress distribution in polycrystalline materials for analyzing local hydrogen accumulation behavior.

In the present study, we established an unprecedented multi-modal three-dimensional (3D) image-based simulation combining the CPFEM and hydrogen diffusion analysis. Fig. 1 shows the summarized flowchart of the X-ray imaging experiments and 3D image-based simulation. To construct a 3D image-based model, the 3D microstructure of a specimen was visualized via X-ray microtomography (XMT) (Kobayashi et al., 2016; Singaravelu et al., 2020) and diffraction contrast tomography (DCT) (Ludwig et al., 2009; Zhao et al., 2020), which allow non-destructive 3D observation of the microstructure. XMT can also visualize deformation and fracture behavior in 4D (3D + time) in the same specimen (Stannard et al., 2018; Su et al., 2019). A multi-modal 3D image-based mesoscale simulation was conducted to bridge nanoscale mechanisms with macroscale fracture behavior in an Al-Zn-Mg alloy. The experimental and image-based simulation results can be directly compared using the proposed imaging technique (Pouillier et al., 2012). The hydrogen concentration in the actual crack propagation region and the amount of hydrogen trapped at each trap site were determined but have not yet been determined. The HE behavior was interpreted based on the simulated hydrogen accumulation in the HE region.

2. Experimental procedure

2.1. Materials

Al-8.4Zn-1.0Mg (mass%) alloy containing iron (Fe < 0.01 mass%) was used in the present study. The ingot was homogenized at 773

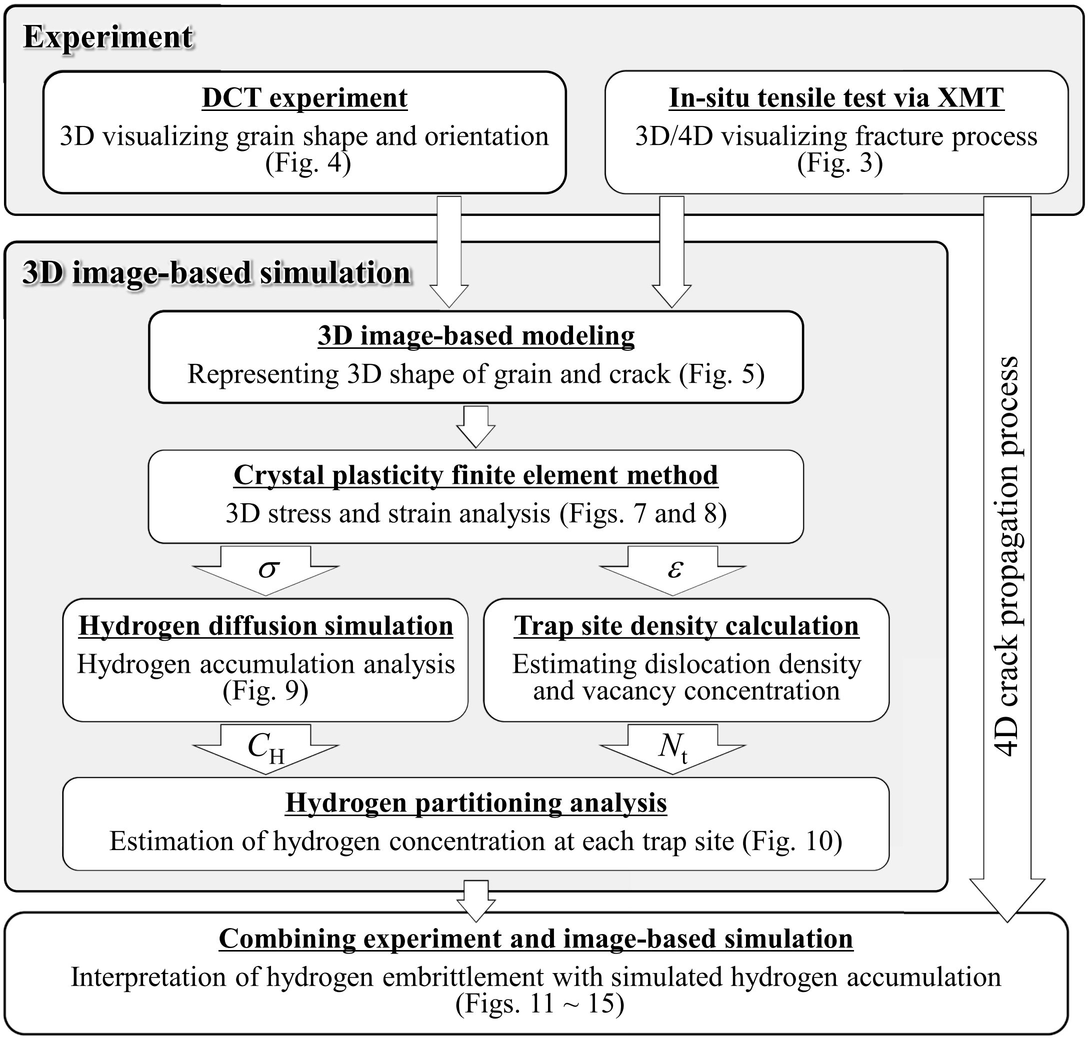

Fig. 1. Flow chart of the present multi-modal 3D image-based simulation combined experiment (3D/4D visualization by XMT and DCT) and image-based simulation.

K for 2 h, and then hot rolled with a rolling reduction of 50 % at 723 K and solution treated at 773 K for 2 h. Immediately after the solution treatment, over-aging treatment was conducted at 393 K for 40 h and 453 K for 7 h. The specimen for the *in-situ* tensile tests was prepared by employing electrical discharge machining (EDM) in water. The specimen's gauge length and cross-sectional area were 0.7 mm and 0.6 mm × 0.6 mm, respectively, the exact dimensions as in the previous work (Su et al., 2019). The machined surface is a fresh aluminum surface without an oxide film. As the electrode wire passes through the metal, an oxide film is immediately formed on the fresh aluminum surface, and hydrogen is generated by reacting aluminum and water (H_2O). According to Young et al. (2002), the nucleated hydrogen evolved in this reaction has an extremely high fugacity of 10^{67} Pa, and hydrogen diffuses into the material. As a result, hydrogen was charged into the specimen by EDM in water, as in Bhuiyan et al. (2016). After EDM, the specimen was stored at room temperature for approximately four days to distribute hydrogen to the specimen's interior, given the hydrogen diffusion coefficient for over-aged Al-Zn-Mg alloy (Young and Scully, 2002). The total hydrogen concentration, measured by a gas chromatography-type thermal desorption analyzer (TDA; PDHA-1000, NISSHA FIS, Inc.), was 1.14×10^{25} atoms H/m^3 (i.e., 7.0 mass ppm).

2.2. Synchrotron radiation X-ray imaging and in-situ tensile testing

The XMT and DCT experiments were carried out at BL20XU in SPring-8, Japan. A monochromatic X-ray beam with 20 and 30 keV X-ray energies was used for the XMT and DCT experiments, respectively. The image detector for the XMT experiment was a 2048 × 2048 pixel element digital CMOS camera with a specimen-to-image detector distance of 20 mm. 1800 transmission images were captured in 0.1° increments over a range of 180°. The DCT experiment image detector consisted of another 2048 × 2048 pixel element digital CMOS camera with a specimen-to-image detector distance of 8 mm to intercept the diffraction spots from the {111}, {200}, and {220} lattice planes of the aluminum alloy. In this case, 3600 images were captured in 0.1° increments over a range of 360°. The effective pixel size of the image detectors for the XMT and DCT experiments were 0.5 and 3.1 μm, respectively.

3D images were reconstructed from the transmission images obtained by XMT by a convolution back-projection algorithm. A linear absorption coefficient of 0 to 40 was collected to fit the 8-bit grayscale from 0 to 255. The Marching Cubes algorithm calculated the center of gravity, volume, surface area, and equivalent diameter of intermetallic compound (IMC) particles and hydrogen micropores in the specimen (Lorensen and Cline, 1987). To suppress the inaccuracies generated by image noise, only IMC particles and hydrogen micropores over 9 voxels in volume were counted as microstructural features. Fig. 2 shows virtual cross-sections of 3D reconstructed images prior to the deformation. The tensile load was applied in the rolling direction.

A small material testing machine (CT500, Deben UK Ltd.) was installed on the rotation stage of the XMT system. The strain rate was set in the tensile test at 3×10^{-3} s^{-1}. The DCT scan was performed without loading, and the XMT scans were performed while holding at an applied strain for 10 min. The fracture surface was observed by a scanning electron microscope (SEM). The fracture surface, crack propagation behavior, and nominal stress−strain response are shown in Fig. 3. Due to the stress relaxation behavior during the XMT scans, vertical drops in the nominal stress are observed in Fig. 3(c). Intergranular, quasi-cleavage, and ductile fracture surfaces were observed. Intergranular cracks were initiated from the specimen surface at an applied strain of 3.2 %, and part of an intergranular crack transitioned to a quasi-cleavage crack at an applied strain of 9.2 %. There was no trace of micro-void on the quasi-cleavage fracture surface, although a typical river pattern appeared. Note that some dimple patterns were visible on the fracture surface, but these were traces of ductile fracture caused by micropores that were already present on the grain boundaries and grain interior at the no-load stage and were not traces of HE behavior.

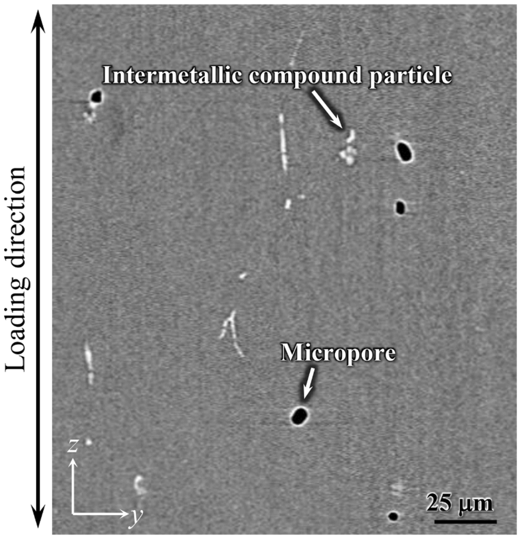

Fig. 2. Virtual cross-sections captured by XMT showing typical distributions of micropores (black), intermetallic compound particles (white).

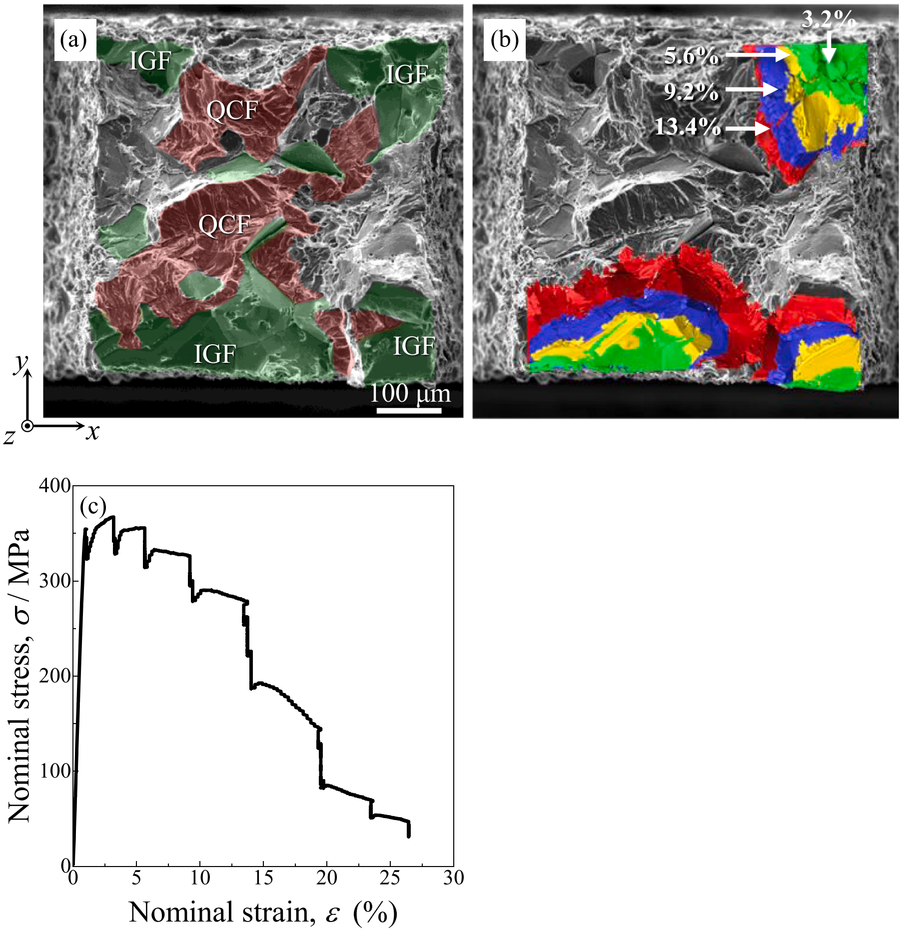

Fig. 3. (a) Fracture surface morphology, (b) crack growth behavior, and (c) nominal stress-nominal strain response of Al-8.4Zn-1.0Mg alloy. In (a), the intergranular and quasi-cleavage fracture regions are indicated in green and red, respectively. In (b), the cracks visualized by the XMT experiment at the various applied strains are shown in green, yellow, blue, and red, along with the nominal strains.

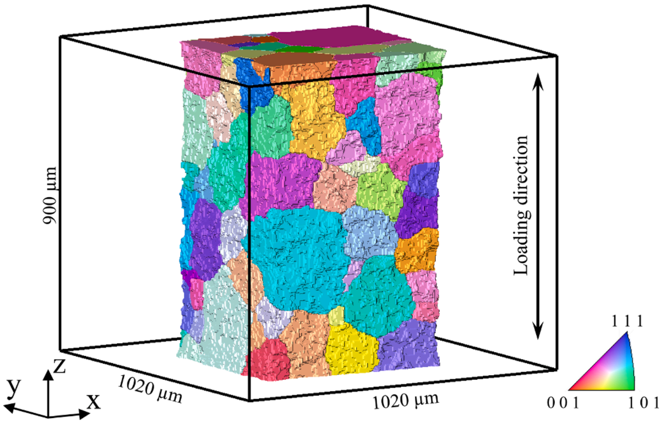

Fig. 4. 3D grain structure and crystallographic orientation of all 155 grains in the gauge section. The color in the 3D image corresponds to the [001] inverse pole figure.

3. Methodology

3.1. 3D image-based modeling

The shape and crystallographic orientation of individual grains were reconstructed by DCT, as shown in Fig. 4. There were 155 grains in the gauge section. To analyze the initiation of the quasi-cleavage crack, a 3D image-based model introducing cracks was constructed. All the cracks in the 3D FEM model were intergranular cracks visualized at an applied strain of 5.6 % (indicated in yellow in Fig. 3 (b)). We recognize that the crack propagation criterion has not been established, even when using modern crystal plasticity models that can also represent crack propagation. Additionally, even with modern methods, quantitatively analyzing crack initiation and propagation via simulation from the initial state is exceedingly complex because (i) the crack propagation criterion varies according to the hydrogen distribution and (ii) the deformation behavior around the crack and work hardening behavior are expected to be completely variable depending on the crack propagation criterion. Therefore, as a realistic approach, we modeled the actual crack morphology observed in the specimen used in the present *in-situ* tensile test.

Fig. 5 shows the constructed 3D image-based simulation model used in the present simulations. First, cracked grain boundaries were identified by overlapping the 3D cracks and grain images obtained in the XMT and DCT experiments. Second, a region of interest was defined around the cracks, and an FEM mesh representing the grain surface (i.e., grain boundary) was constructed using a triangular two-dimensional (2D) mesh. Third, to create an FEM mesh that reproduced the upper and lower cracked surfaces, the grain boundary area containing the intergranular crack was separated from the remaining unfractured grain boundary. Fourth, the nodes and elements in the cracked region were duplicated on the upper and lower crack surfaces, and only the duplicated nodes associated with the crack tips were merged with the original nodes. It should be noted that the reproduced crack tip in the FEM model was sharp in this process. A mesh of 3D grains with quadratic tetrahedral elements was then built from the triangular mesh at the boundary. The above explanation involves how to construct the model of the grains, which are colored in the center of the model shown in Fig. 5, in the region of interest. Finally, the specimen geometry was reproduced in the FEM model using quadratic tetrahedral elements by the following process to apply a load to the grain model. The specimen surface was reproduced with triangular 2D mesh from XMT images. Areas on the specimen surface other than the area set as the region of interest were extracted. This area is associated with the gray part in Fig. 5. A 3D mesh of the specimen interior with quadratic tetrahedra was automatically built from a closed 2D element set composed of the specimen surface and grain surface inside the specimen. Note that the 3D grain shape was reproduced only in the region of interest in the center of the model. In 3D regions other than the region of interest, for associating each element with the grains, the gravity center of each element was compared with the 3D grain image to determine which element was located inside the grain interior. Each grain was then treated as consisting of associated elements. The crystallographic orientations, which were obtained by the DCT experiment, were assigned to all the elements. The initial state of the simulation model was the same as the state in which the applied stress was unloaded from an applied strain of 5.6 % in the experiment. Khoei et al. (2015), analyzed the mode I stress intensity factor (SIF) using models with varying ratios of crack length and element size and reported that the SIF converges if the mesh size is less than 5 % of the crack length using a model configured with polygonal elements. Given this, we determined the minimum mesh size at

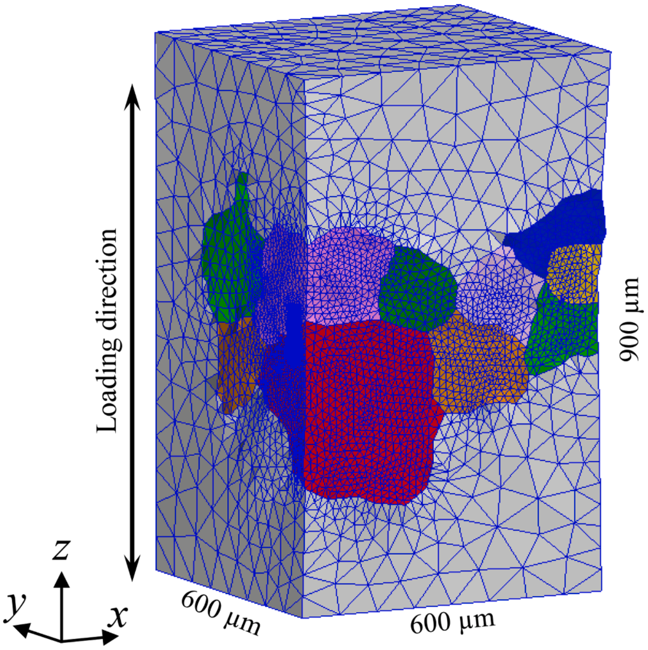

Fig. 5. Finite element mesh representation of the grain microstructure in the gauge section of the specimen, determined by DCT experiment as shown in Fig. 4.

the crack tip to be 2 μm, as the crack length was 50–100 μm at an applied strain of 5.6 %.

3.2. Crystal plasticity finite element method

In the present study, the effect of the hydrogen concentration distribution around the crack tip, which changed while holding at an applied strain, on crack propagation was evaluated. CPFEM and hydrogen diffusion analyses were not coupled but were performed independently of each other, as shown in Fig. 1. To analyze the plastic deformation behavior, the classical viscoelastic plasticity-type CPFEM was employed in the present study to consider the interactions among grains. Recently, a dislocation density-based crystal plasticity formulation was developed that allows more physical interpretation of the results (Gao et al., 2023; Jiang et al., 2022; Khan et al., 2015; Mayama et al., 2009). One major issue in analyses using dislocation density-dependent models is that the actual distribution of dislocation density in the material is heterogeneous, making it difficult to reproduce the initial dislocation density. Determining the initial dislocation density is mainly used as a fitting parameter to represent macroscopic behavior rather than the actual dislocation density distribution; this is also why none of the studies have rigorously measured the distribution of dislocation density in materials or compared it with the results of crystal plasticity analysis using a dislocation density-based hardening law. Using a roughly approximated dislocation density to estimate the interaction with hydrogen does not accurately represent the behavior in actual materials. At present, there can be no essential difference between the results of analyses using the phenomenological hardening law and those using the dislocation density-dependent hardening law. The following models were incorporated into ABAQUS via the user-defined material (UMAT) subroutine developed by Huang (1991). The total deformation gradient $\boldsymbol{F}$ can be multiplicatively decomposed as follows (Asaro and Rice, 1977; Kröner, 1959; Lee and Liu, 1967; Peirce et al., 1983):

$$\boldsymbol{F} = \boldsymbol{F}_{\mathrm{e}}\boldsymbol{F}_{\mathrm{p}} \tag{1}$$

where $\boldsymbol{F}_{\mathrm{e}}$ is the elastic part of the deformation gradient that describes the elastic deformation and lattice rotation, and $\boldsymbol{F}_{\mathrm{p}}$ is the plastic part of the deformation gradient due to crystallographic slip. The plastic velocity gradient $\boldsymbol{L}_{\mathrm{p}}$ is expressed as:

$$\boldsymbol{L}_{\mathrm{p}} = \dot{\boldsymbol{F}}_{\mathrm{p}}\boldsymbol{F}_{\mathrm{p}}^{-1} = \sum_{\alpha=1}^{N} \dot{\gamma}^{(\alpha)}\left(\boldsymbol{m}^{(\alpha)} \otimes \boldsymbol{n}^{(\alpha)}\right) \tag{2}$$

where $\dot{\gamma}^{(\alpha)}$ is the slip rate on the slip system α, and $\boldsymbol{m}^{(\boldsymbol{\alpha})}$ and $\boldsymbol{n}^{(\boldsymbol{\alpha})}$ are the slip direction and slip plane normal of the slip system, respectively. The slip rate on each slip system, as described below, depends on the resolved shear stress, $\tau^{(\alpha)}$, and the slip resistance, $g^{(\alpha)}$, of the slip system (Hutchinson, 1976; Pan and Rice, 1983; Peirce et al., 1983):

$$\dot{\gamma}^{(\alpha)} = \dot{\gamma}_0 \left[\frac{\tau^{(\alpha)}}{g^{(\alpha)}}\right] \left|\frac{\tau^{(\alpha)}}{g^{(\alpha)}}\right|^{n-1} \tag{3}$$

where $\dot{\gamma}_0$ is the reference value of the slip rate, and n is the rate sensitivity exponent. The evolution of the slip resistance $\dot{g}^{(\alpha)}$ can be expressed as follows (Zhou et al., 1993):

$$\dot{g}^{(\alpha)} = \sum_{\beta=1}^{n} h_{\alpha\beta}\left|\dot{\gamma}^{\beta}\right| \tag{4}$$

where $h_{\alpha\beta}$ is a hardening matrix that represents the interaction between slip systems α and β (Zhou et al., 1993). Peirce et al. (1982) developed the following equation for the self-hardening matrix ($\alpha = \beta$):

$$h_{\alpha\alpha} = h(\gamma) = h_0 \mathrm{sech}^2\left|\frac{h_0\gamma}{\tau_{\mathrm{s}} - \tau_0}\right| \tag{5}$$

where h_0 is the initial hardening modulus, τ_{s} is the stage-I stress, and τ_0 is the yield stress, which equals the initial slip resistance, $g^{(\alpha)}(0)$. In Eq. (5), γ is the total accumulated shear slip strain on all the slip systems, which is defined as follows (Peirce et al., 1982):

Table 1
Material parameter values for crystal plasticity.

Anisotropic elastic modulus	C_{11} [GPa]	106
	C_{12} [GPa]	60.7
	C_{44} [GPa]	28.2
Initial yield stress	τ_0 [MPa]	125
Stage-I stress	τ_s [MPa]	145
Initial hardening modules	h_0 [MPa]	145
Latent hardening coefficient	q	1.0
Rate sensitivity exponent	n	12
Reference strain rate	$\dot{\gamma}_0$	1×10^{-3}

$$\gamma = \sum_{\alpha} \int_{0}^{t} \left| \dot{\gamma}^{(\alpha)} \right| dt \tag{6}$$

The latent hardening matrix ($\alpha \neq \beta$) is given by the following (Hutchinson, 1976; Peirce et al., 1982):

$$h_{\alpha\beta} = qh(\gamma) + (1-q)h(\gamma)\delta_{\alpha\beta} \tag{7}$$

where q and $\delta_{\alpha\beta}$ are the latent hardening coefficient and the Kronecker delta, respectively.

The material parameters used in the present analysis are listed in Table 1. The anisotropic elastic moduli of C_{11}, C_{12}, and C_{44} were adopted from Kobayashi et al. (2016). The rate sensitivity exponent, n, in predicting stress-strain behavior is significance (Liu et al., 2021; Liu and Dunne, 2021). A comprehensive quantitative analysis, incorporating velocity dependence, should be conducted. However, it's important to note that such an analysis extends beyond the scope of the present study. So, we employed a value of n in the present analysis by referencing its application in previous CPFEM studies on aluminum alloy (Kobayashi et al., 2016). The initial yield stress, τ_0, stage-I stress, τ_s, initial hardening modulus, h_0, latent hardening coefficient, q, and reference strain rate, $\dot{\gamma_0}$, were calibrated by comparing the experimental stress−strain relationship in Fig. 6 and the calculated stress−strain relationship obtained by the CPFEM. The analysis model used in the calibration is a polycrystalline model consisting of 1000 grains, as shown in Fig. 6 (a), where initial crystal orientations are selected from experimentally obtained texture data. Each grain is divided into 3 × 3 × 3 elements to reproduce intragranular heterogeneity. In Fig. 6 (c), the red line shows the stress−strain curve calculated by the CPFEM with the material parameters in Table 1. The experimental stress−strain behavior before crack initiation at an applied strain of 3.2 % was well reproduced by the present analysis except for a sudden decrease in stress owing to stress relaxation during the XMT scans. Based on the above comparisons, it was confirmed that by employing the parameters in Table 1, the CPFEM could successfully reproduce the experimental results. These parameters were used in the present study. The material used in the present study is a precipitation-strengthened alloy, and the presence of precipitates affects the mechanical properties of the alloy. The influence of the presence of precipitates on the mechanical properties was indirectly incorporated into the CPFEM by using calibrated parameters reproducing the macroscopic properties.

In the present study, we investigated the effects of stress, strain, and hydrogen accumulation on HE crack propagation behavior when strain was applied from 5.6 % to 7.6 %. The stress/strain distribution at an applied strain of 5.6 % was evaluated via mechanical analysis via the CPFEM. However, there were care points to keep in mind about the initial state of the simulation model: (i) the 3D grain shape was reproduced based on the 3D grain image at the unloading state, and (ii) the model incorporates the crack shape at an applied strain of 5.6 %. From these points, it is reasonable to assume that the initial state of the simulation model corresponds to the condition where the load was removed from the situation at an applied strain of 5.6 % in the experiment. Thus, applying enforced displacements to the model until the macroscopic stress response corresponds to the stress at 5.6 % strain in the experiment can be regarded as the target state of the mechanical analysis. Conducting the above assumption, an enforced displacement of up to 1.8 % in the z-direction was applied to the simulation model in the present analysis. Note that the state after applying displacement to the model corresponds to the state with an applied strain of 5.6 % in the experiment, not 7.4 %.

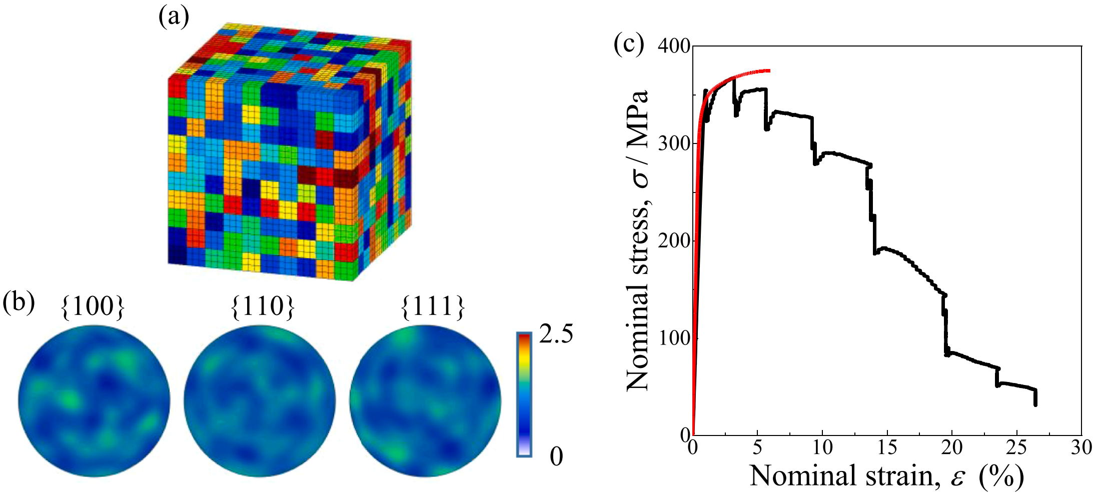

Fig. 6. (a) The analysis polycrystalline model consisted of 1,000 grains based on experimentally measured texture and (b) pole figure of the used model. (c) Nominal stress-strain response obtained by the *in-situ* tensile test and CPFEM using polycrystalline model (a) with the material parameters in Table 1.

3.3. Hydrogen diffusion analysis

The respective gradients of hydrostatic stress act as driving forces for hydrogen diffusion (Isfandbod and Martínez-Pañeda, 2021). In the present study, we used the following hydrogen diffusion model, taking into account the change in chemical potential due to hydrostatic stress, proposed in (Li et al., 1966; Sofronis and McMeeking, 1989):

$$\frac{\partial C_{\mathrm{H}}}{\partial t} = D_{\mathrm{H,\ eff}} \nabla^2 C_{\mathrm{H}} - \nabla\left(\frac{D_{\mathrm{H,\ eff}} C_{\mathrm{H}} \overline{V}_{\mathrm{H}}}{RT} \nabla \sigma_{\mathrm{h}}\right) \tag{8}$$

where C_{H} is the diffusible hydrogen concentration, $\overline{V}_{\mathrm{H}}$ is the partial molar volume of hydrogen, R is the gas constant, T is the absolute temperature, and σ_{h} is the hydrostatic stress. $D_{\mathrm{H,\ eff}}$ is the effective hydrogen diffusion coefficient, which includes the effect of hydrogen trapping and detrapping behavior of all trap site in material. In the present analysis, we employed $D_{\mathrm{H,\ eff}} = 1.1 \times 10^{-11}$ m^2/s, which applies to over-aged Al-Zn-Mg alloy, as reported by Young et al. (2002). The second term in Eq. (8) indicates the effect of the hydrostatic stress distribution on hydrogen diffusion. The code for hydrogen diffusion analysis was developed independently (Ebihara et al., 2011) and we solved Eq. (8) by the finite volume method.

In aluminum alloys, since hydrogen is most stable in the molecular state in the micropore (Yamaguchi et al., 2018), it can be predicted that molecular hydrogen remains in micropores instead of diffusing into the aluminum matrix. In the present study, the total hydrogen concentration (i.e., 1.14×10^{25} atoms H/m^3 (7.0 mass ppm)), measured by TDA, minus the molecular hydrogen

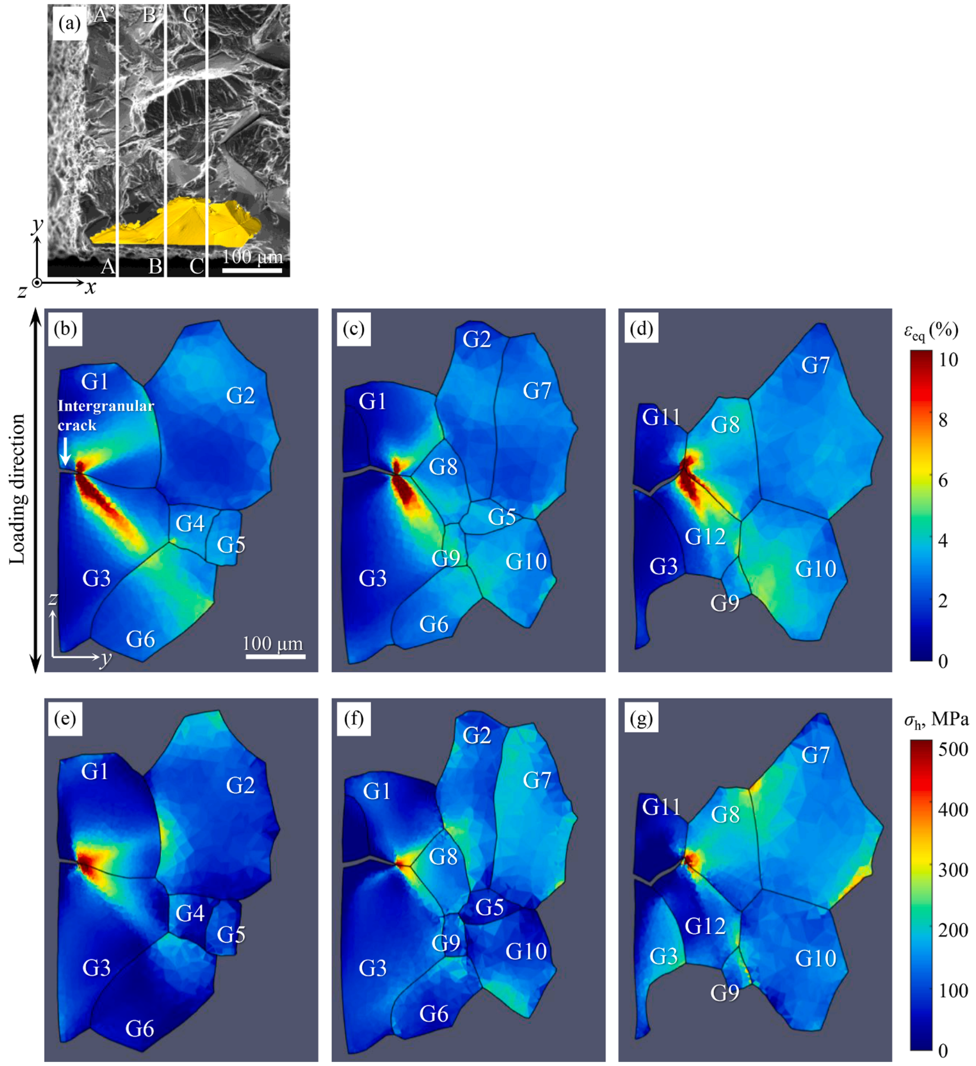

Fig. 7. (a) Magnified SEM image of the fracture surface shown in Fig. 3, and visualization of the crack captured by XMT at $\varepsilon_{\mathrm{apply}} = 5.6$ %. The captured cracks, indicated in yellow, are superimposed on the fracture surface. (b)–(d) Equivalent plastic strain distribution, and (e)–(g) hydrostatic stress distribution, along cross-sections A-A', B-B' and C-C', which are shown as white solid lines in (a).

concentration in micropores was adopted as the diffusible hydrogen concentration, C_{H}. The molecular hydrogen concentration in a micropore, $C_{\mathrm{Pore,\ H_2}}$, is expressed as follows.

$$C_{\mathrm{Pore,\ H_2}} = \sum 2N_A \frac{4\gamma_{\mathrm{s}} V_i^{\mathrm{pore}}}{d_i^{\mathrm{pore}} RT} \tag{9}$$

where N_A is Avogadro's constant; γ_{s} is the surface energy of aluminum; and V_i^{pore} and d_i^{pore} are respectively the volume and equivalent diameter of a micropore. The micropore's volume and equivalent diameter were calculated from 3D images of the XMT experiment. The total molecular hydrogen concentration in all the micropores was 7.36×10^{22} atoms H/m^3 (i.e., 0.05 mass ppm). Hence, the diffusible hydrogen concentration, C_{H}, can be calculated as 1.13×10^{25} atoms H/m^3 (6.9 mass ppm). To exactly estimate the hydrogen distribution, a model that includes the effect of the history of crack propagation and hydrogen distribution should be employed. However, employing this model results in low accuracy because of the following challenging issues: (i) uncertainty in the crack propagation model and (ii) difficulty in quantifying the hydrogen-induced crack propagation criterion. If these issues are solved, a more accurate analysis can be conducted to elucidate the hydrogen-induced crack propagation behavior. To prevent loss of accuracy due to the introduction of uncertainty factors, in the present analysis, a uniform distribution of hydrogen was set in the initial state.

The hydrogen diffusion behavior was analyzed under the 3D hydrostatic stress distribution calculated by the CPFEM. The hydrostatic stress is crucial when hydrogen diffusion analysis is performed under stress. Generally, in the FEM, stress and strain values are calculated at Gauss points in the elements. These values are more accurate at Gauss points than at nodes because nodal solutions are interpolated based on the surrounding Gauss points. Therefore, in the present analysis, the nearest Gauss point to each element node was used to ensure the accuracy of the stress values, and the hydrostatic stress value at the Gauss point was assigned to that node. This process was conducted for all the element nodes. Note that the accuracy of the spatial distribution decreases as the size of the element increases via this process. However, in the present study, the spatial error was less than 2 μm around the crack tip.

4. Numerical simulation results

Fig. 7 shows the 3D equivalent strain and hydrostatic stress distributions obtained by the CPFEM and the magnified SEM image of the fracture surface, where the equivalent plastic strain, $\varepsilon_{\mathrm{eq}}$,was calculated by time integration of the following equation:

$$\dot{\bar{\varepsilon}}^{\mathrm{p}} = \sqrt{\frac{2}{3}\boldsymbol{D}^{\mathrm{p}} : \boldsymbol{D}^{\mathrm{p}}} \tag{10}$$

where $\boldsymbol{D}^{\mathrm{p}}$ is plastic strain rate tensor which is derived from symmetric part of plastic velocity gradient tensor $\boldsymbol{L}_{\mathrm{p}}$. In Fig. 7, a heterogeneous distribution of strain and stress appeared. Both the strain and stress localized regions were particularly observed at cross-section A-A' (the solid white line in Fig. 7 (a)). The stress and strain localization were attributed to the interactions among grains, specifically, the difference in the deformation resistance of individual grains (Toda et al., 2016; Tondro and Abdolvand, 2022). To assess the heterogeneous plastic deformation behavior, the local Taylor factors were calculated using the average value of the equivalent strain and the crystallographic orientation, as described in Toda et al. (2016). The local Taylor factor of a grain reflects the plastic deformation behavior, which is attributable to the activity of slip systems. This factor was calculated to compare the tendency for slip deformation among numerous grains using local strain values and crystallographic orientation. The deformation rate tensor was calculated from the strain in individual grains obtained by the CPFEM. The strain values were averaged for each grain. The local Taylor factor was subsequently calculated such that five slip systems that minimized the internal work became operative for an associated strain increment. The local Taylor factor corresponds to the deformation resistance when the multiple slip system is activated. Previous studies (Toda et al., 2016) have shown that high-strain regions tend to be located between grains with significant differences in local Taylor factors, and they reported that the mismatch in deformation caused by the difference in deformation resistance leads to this strain localization around the grain boundary. Assuming that the Taylor factor corresponds to the deformation

Table 2
Summary of the local Taylor factors of individual grains around the intergranular crack shown in Fig. 7.

Grain No.	Local Taylor factor, M
1	2.40
2	3.61
3	3.13
4	4.59
5	3.84
6	2.19
7	3.61
8	2.40
9	3.52
10	2.91
11	3.54
12	2.65

resistance, in the present study, the influence of differences in the deformation resistance between neighboring grains on the plastic strain distribution is discussed. Table 2 shows the local Taylor factors of the 12 grains shown in Fig. 7. Although grain 1 had a lower resistance to plastic deformation than grain 3, the equivalent strain accumulated in grain 3. The localized plastic strain region in cross-section A-A' was extended due to grain 6, which has the lowest local Taylor factor. However, grain 2, which was in contact with grain 1, had a relatively high local Taylor factor and thus may have inhibited the plastic deformation of grain 1. The deformation interaction caused by the difference in local Taylor factors among neighboring grains led to remarkable strain localization around the crack tip in grain 1. As shown in Fig. 7 (c) and (d), both the strain localization around the grain boundaries and the strain distribution ahead of the crack tip were due to the difference in the resistance to plastic deformation among the surrounding grains.

The hydrostatic stress tended to be high in the region with a high plastic strain gradient. The maximum hydrostatic stress, more than 1.25 GPa, was in the vicinity of the crack tip as shown in Fig. 8. The cross-section A-A' is in the vicinity of the region that the crack bent towards. Assuming that the main crack was a combination of several minor cracks propagating in different directions, the cumulative hydrostatic stress in the crack juncture region would be higher than that of the individual minor cracks. Therefore, the stress distribution ahead of the crack tip was remarkably high at the cross-section A-A', as shown in Fig. 7 (e). In all the grains except for the grains 1, 3, and 8, which were in contact with the crack tip, the hydrostatic stress was concentrated more around the grain boundary than within the grain interior. The hydrostatic stress field was found to be propagated from the crack tip, across the grains 7 and 8, at the cross-section C-C' (Fig. 7 (g)). This stress-concentrated region was formed by the stress associated with the crack and the stress concentration in the upper section of the boundary between the grains 7 and 8.

In contrast to the initial uniform hydrogen concentration, after 10 min of applied stress, hydrogen was accumulated, corresponding to the distribution of hydrostatic stress, as shown in Fig. 7. Fig. 9 shows the hydrogen distribution, after 10 min (i.e., the displacement holding time) of applied stress, at the *y*-*z* cross-section where the quasi-cleavage crack was initiated (i.e., A-A' in Fig. 7 (a)). Hydrogen significantly accumulated around the crack tip where hydrostatic stress is high, as shown in Fig. 7 (e). The hydrogen concentration increased to more than 1.5 times the initial concentration in a region limited within 5 μm from the crack tip, and the maximum hydrogen concentration reached 2.0×10^{25} atoms H/m^3 (i.e., 12.2 mass ppm; 1.75 times the initial hydrogen concentration). Hydrogen concentration was distributed with a peak at a position about a few micrometers from the crack tip. The solid white line in Fig. 9 (b) represents a cross-section of the crack shape at an applied strain of 9.2 %, superimposed on the hydrogen distribution in the magnified region (framed in black in Fig. 9 (a)). The crack propagated into a moderate hydrogen concentration region near the grain boundary rather than the high hydrogen concentration region.

5. Discussion

Quantitative analysis of the dynamic behavior of hydrogen partitioning to the precipitate interface is necessary in order to discuss quasi-cleavage crack initiation. The total hydrogen concentration, i.e., the sum of the concentration of hydrogen trapped at the interstitial lattice site and the various trap sites is expressed as follows (Isfandbod and Martínez-Pañeda, 2021; Shimizu et al., 2019; Su et al., 2019):

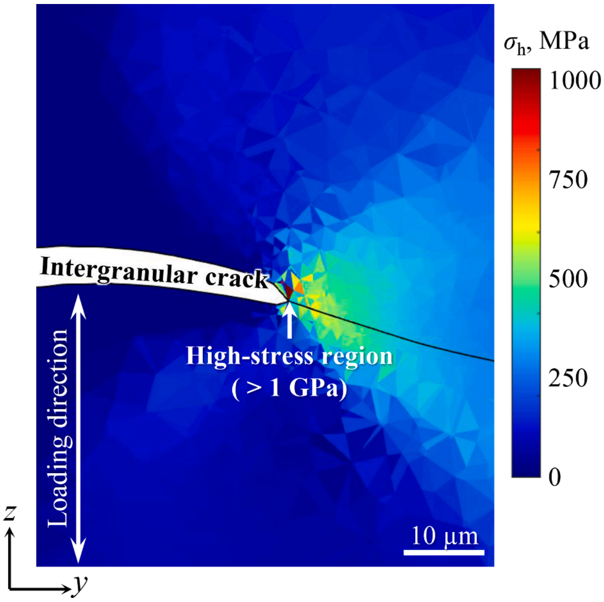

Fig. 8. The distribution of hydrostatic stress (elemental value) at the cross-sections having maximum hydrostatic stress region, which is located between cross-section of A-A' and B-B' in Fig. 7 (a).

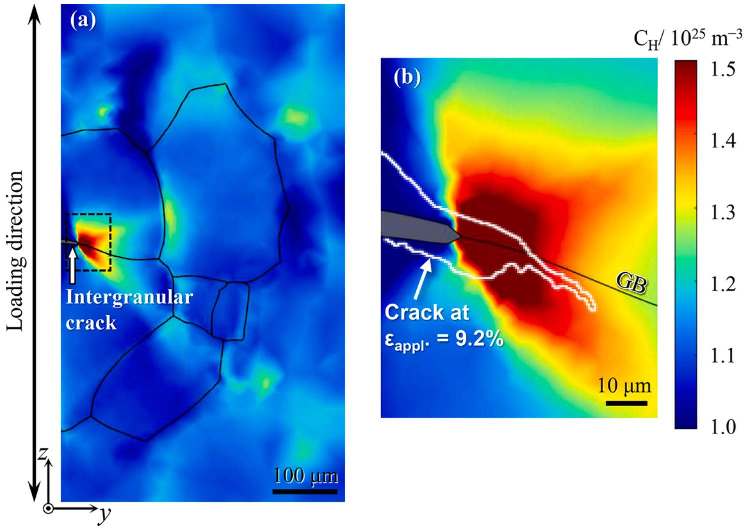

Fig. 9. (a) Hydrogen distribution, after 10 min of applied stress, at the *y-z* cross-section where the quasi-cleavage crack initiated. (b) Hydrogen distribution in the magnified region (framed in white in (a)) superimposed on a cross-sectional image of the crack shape at $\varepsilon_{\text{apply}} = 9.2$ %.

$$C_{\text{H}} = C_L + \sum C_i = \theta_L N_L + \sum \theta_i N_i \tag{11}$$

where C_L and C_i is the concentration of hydrogen at the interstitial lattice site and *i*th trap site. θ_L is the hydrogen occupancy of the interstitial lattice site and θ_i is the occupancy of *i*th trap site. N_L and N_i are the trap site densities in the interstitial lattice site and the *i*th trap site. When hydrogen concentration increases, the concentration of hydrogen trapped at each trap site, C_L and C_i, also increases. According to Oriani (1970), hydrogen occupancy of each trap site can be calculated by assuming that hydrogen trapped at the interstitial lattice site and other trap sites is in a local equilibrium state as follows:

$$\frac{\theta_i}{1-\theta_i} = \theta_{\text{L}} \exp\left(\frac{E_{\text{b},i}}{RT}\right) \tag{12}$$

where $E_{\text{b},i}$ is the hydrogen trap energy of an *i*th trap site. In the initial state (i.e., before loading), hydrogen is partitioned to each trap site in accordance with the initial hydrogen concentration, trap site density, and the trap energy of each trap site, according to Eqs. (11) and (12). After loading, the concentration of hydrogen trapped at trap sites changes due to the hydrogen accumulation behavior and the increased trap site density of vacancies and dislocations (Krom et al., 1999; Shimizu et al., 2020, 2019; Su et al., 2019). By determining the hydrogen concentration, trap site density, and the binding energy after loading, the hydrogen occupancy of each trap site can be numerically calculated from Eqs. (11) and (12). In the present study, C_{H} (on the left side of Eq. (11)) was defined as the hydrogen concentration at each node after 10 min of applied stress. The hydrogen trap sites in the Al-Zn-Mg alloys used in this study were vacancies, dislocations, grain boundaries, precipitate interfaces, and micropores (Ismer et al., 2009; Tsuru et al., 2018; Yamaguchi et al., 2021, 2019, 2018). The hydrogen trap energies have been analyzed by first-principles calculations and are summarized in Table 3 (Ismer et al., 2009; Shimizu et al., 2024; Tsuru et al., 2018; Yamaguchi et al., 2021, 2019, 2018).

To quantitatively analyze trap site densities, the dislocation density, vacancy concentration, fractional area of the grain boundary and precipitate, and micropore surface areas were calculated from experiments, simulations, and mathematical models (Shimizu et al., 2020, 2019; Su et al., 2019). Details regarding the quantification of the trap site densities (other than that of the grain boundary) have been provided in our previous studies (Shimizu et al., 2020, 2019; Su et al., 2019). The increase in vacancies and dislocations during deformation is much greater than that at the order level. The influence of slight differences in trap site density other than dislocations and vacancies on the hydrogen partitioning analysis is quite limited. Therefore, in the present analysis, we analyzed the increase in the

Table 3
Summary of the hydrogen trap energies derived by first-principles calculation.

Trap site	Binding energy, E_{b} (kJ/mol)	Refs.
Vacancy	28.9	Ismer et al. (2009)
Screw dislocation	10.6	Yamaguchi et al. (2021)
Edge dislocation	17.4	Yamaguchi et al. (2021)
Grain boundary	19.3	Yamaguchi et al. (2019)
Precipitate (Coherent interface)	8.6–32.6	Tsuru et al. (2018)
Precipitate (Semi-coherent)	53.8	Shimizu et al. (2024)
Pore (Surface H)	67.5	Yamaguchi et al. (2018)

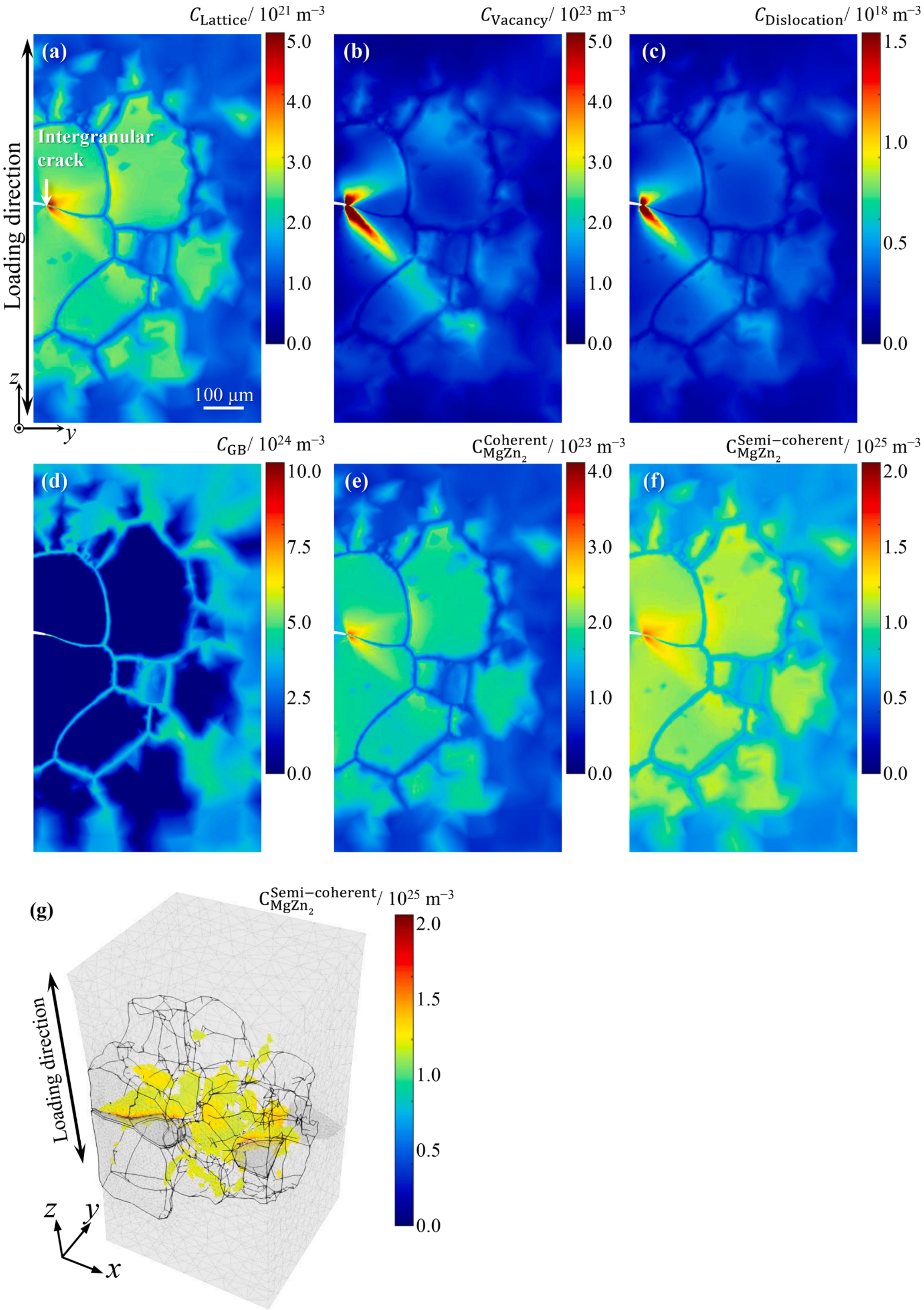

Fig. 10. The hydrogen partitioning behavior after 10 min of applied stress, showing the distribution of hydrogen trapped at the (a) interstitial lattice site, (b) vacancy, (c) dislocation, (d) grain boundary, (e) coherent interface of precipitate, and (f) semi-coherent interface of precipitate, respectively. (g) 3D distribution of hydrogen concentration trapped at semi-coherent interface of precipitate. The region where hydrogen concentration is more than 1.15×10^{25} atomH/m^3 were visualized. Black lines represent the triple junction in the specimen.

trap site density of vacancies and dislocations. The trap site densities of the grain boundaries, precipitates, and micropores were therefore estimated from the microstructure before loading. The fractional area of the precipitate interface, obtained from TEM and reported by Bendo et al. (2018a, 2018b), was used in the present analysis. The surface area of the micropores was measured using a reconstructed 3D image obtained by the XMT experiment. To estimate the trap site density of the grain boundary, the local fractional area of the grain boundary, F_{GB}, was calculated as the area divided by the volume of the grain boundary. Assuming that the volume is equal to the product of the area and the thickness of the grain boundary, the fractional area is equal to the reciprocal of the grain boundary thickness. The thickness of grain boundary in aluminum was determined by common neighbor analysis to be $t_{\mathrm{GB}} = 0.54$ nm (Shimokawa et al., 2005).

The increment in vacancy concentration under loading can be calculated from the local strain rate and dislocation density distribution (Militzer et al., 1994; Shimizu et al., 2020; Su et al., 2019). Huang et al. (2004) reported the total dislocation density, ρ, under loading to be the sum of the statistically stored dislocation (SSD) density, ρ_{SSD}, and the geometrically necessary dislocation (GND) density, ρ_{GND}, as follows (Su et al., 2019):

$$\rho = \rho_{\mathrm{SSD}} + \rho_{\mathrm{GND}} \tag{13}$$

SSD tend to accumulate by trapping other dislocations in a random way (Ashby, 1970). Brinckmann et al. (2006) proposed the calculation of SSD density as follows:

$$\rho_{\mathrm{SSD}} = \frac{\sqrt{3}\bar{\varepsilon}^{\,\mathrm{p}}}{bl} \tag{14}$$

where $\bar{\varepsilon}^{\,\mathrm{p}}$ is the equivalent plastic strain, b is the Burgers vector (0.286 nm) and l is the mean free path of dislocation motion, which is half of the single dislocation slip distance (Ohashi et al., 2007; Su et al., 2019). Nye (1953), Ashby (1970) showed that the density of GND can be calculated by the equivalent plastic strain gradient, η_p, with the following equation:

$$\rho_{\mathrm{GND}} = \bar{r}\frac{\eta_p}{b} \tag{15}$$

where $\bar{r}$ is the Nye factor (1.9 in face center cubic alloys (Martínez-Pañeda et al., 2016)). The distributions of SSD and GND calculated from the equivalent strain distribution simulated by the CPFEM in the present analysis.

Militzer et al. (1994) proposed a numerical model that shows the excess vacancy concentration, $C_{\mathrm{v}}^{\mathrm{ex}}$, as follows:

$$C_{\mathrm{v}}^{\mathrm{ex}} = C_{\mathrm{v}}^{0} + C_{\mathrm{v}}^{s}\left(1 - \exp\left[-D_{\mathrm{V}}\left\{\frac{\rho}{\kappa^2} + \frac{1}{L^2}\right\}t_{\mathrm{tens}}\right]\right) \tag{16}$$

where $C_{\mathrm{v},\ 0}$ is the initial vacancy concentration, D_{v} is the vacancy diffusivity, $(1.2 \times 10^{-16}$ m^2/s at 300 K (Carling et al., 2000)), ρ is the dislocation density, $\kappa = 1$ is a parameter representing the distribution of dislocations, L is the grain size, and t_{tens} is the load application time. C_{v}^{s} is the steady-state vacancy concentration and it calculated by following equation (Militzer et al., 1994):

$$C_{\mathrm{S}} = \frac{\chi\sigma}{Q_{\mathrm{f}}}\left(\frac{\rho}{\kappa^2} + \frac{1}{L^2}\right)^{-1}\frac{\Omega_0}{D_{\mathrm{V}}}\dot{\varepsilon} \tag{17}$$

where $\chi = 0.1$ is the dimensionless constant (Militzer et al., 1994), σ is the flow stress, Ω_0 is the atomic volume, Q_{f}=0.55 eV is the formation energy of vacancy (Enomoto et al., 2010) and $\dot{\varepsilon}$ is the strain rate. For XMT scanning, it was necessary to hold the displacement.

The number of hydrogen atoms that a trap site can trap per unit number, unit length, and unit area (herein called the hydrogen trap interval) has been analyzed using first-principles calculations. The hydrogen trap intervals are 1.0 atomH/nm for edge dislocation (Yamaguchi et al., 2021), 1.2 atomH/nm for the screw dislocation (Yamaguchi et al., 2021), 8 atomH/vacancy for the vacancy (Ismer et al., 2009), 21.9 atomH/nm^2 for the grain boundary (Yamaguchi et al., 2019), 17.1 atomH/nm^2 for the coherent interface of precipitate (Tsuru et al., 2020, 2018), 25 atomH/nm^2 for the semi-coherent interface of precipitate (Shimizu et al., 2024), and 20 atomH/nm^2 for the micropore (Yamaguchi et al., 2018). Finally, the trap site density of each trap site can be included by taking the product of the calculated value (e.g., dislocation density) and associated hydrogen trap interval.

Fig. 10 shows the distributions of hydrogen trapped at various trap sites along the y-z cross-section where the quasi-cleavage crack initiated, specifically at the (a) interstitial lattice site, (b) dislocation, (c) vacancy, (d) grain boundary, (e) coherent interface, and (f) semi-coherent interface of the $\mathrm{MgZn_2}$ precipitate. The accumulated hydrogen was mainly repartitioned to the vacancy and $\mathrm{MgZn_2}$ precipitate interface around the crack tip because these sites have a relatively high hydrogen trap energy and trap site density (Ismer et al., 2009; Shimizu et al., 2024; Tsuru et al., 2018). Fig. 10 (g) shows the 3D distribution of hydrogen trapped at the semi-coherent interface of the precipitate. The region where the hydrogen concentration was more than 1.15×10^{25} atomH/m^3 was visualized. Like in the case of the hydrogen distribution, as shown in Fig. 9, the partitioned hydrogen concentration also increases ahead of the crack tip and around a specific grain boundary. At the grain boundary, there is another trap site (i.e., grain boundary) in addition to the trap sites in the grain interior. The partitioned hydrogen concentrations at each trap site at the grain boundary are lower than those at the grain interior if the trap site densities other than the grain boundary and the hydrogen concentration are the same. Therefore, the concentration of hydrogen trapped at trap sites other than the grain boundaries relatively decreased on the grain boundaries, as shown in Fig. 10. The distribution of hydrogen trapped at the interstitial lattice site and the precipitate interface was correlated with the total hydrogen concentration, as shown in Fig. 10 (a), (e), and (f). The distribution of hydrogen trapped at the vacancy and dislocation was correlated with the strain distribution, not the hydrogen distribution, as shown in Fig. 10 (b) and (c); this was caused by the increasing number of vacancies and dislocations corresponding to the plastic stress distribution.

Here, we discuss the contributions of various HE mechanisms to the occurrence of quasi-cleavage fracture based on hydrogen partitioning behavior. As already mentioned, HELP, HEDE, HESIV and their mixed models have been proposed as HE mechanisms. In the Al-Zn-Mg alloy used in the present study, there is an additional mechanism of accelerated HE fracture due to the interfacial debonding behavior of the $MgZn_2$ precipitates. HELP, HEDE, and HESIV are attributed to the interactions of hydrogen with dislocations, interstitial sites, and vacancies, respectively. The maximum hydrogen occupancies of the lattice, dislocations, and vacancies were 2.7×10^{-8}, 9.1×10^{-6}, and 2.9×10^{-3}, respectively, indicating that the amounts of hydrogen partitioned to these trap sites was still low after loading.

Oriani et al. (1974) reported an 40 % decrease in cohesive strength when the hydrogen concentration was 10^4 times the equilibrium concentration in 4340 steel. This calculation indicated that HEDE mechanisms are feasible when the concentration of hydrogen trapped at associated trap sites is extremely high. Realistically, hydrogen concentrations could not reach such high levels. According to Birnbaum et al. (1994) more than 10^{-3} hydrogen atoms per solvent atom are necessary for the HELP mechanism to produce the effect of hydrogen on dislocation mobility. However, the hydrogen occupancy of dislocations is 9.1×10^{-6}, even at the maximum. Therefore, the HEDE and HELP mechanisms did not appear to significantly contribute to the HE in Al-Zn-Mg alloys. These differences occur because these trap sites have low trap energies in Al-Zn-Mg alloys. Therefore, in the case of, for example, pure metals and other alloys without strong trap sites such as $MgZn_2$ precipitates, the hydrogen concentration partitioned to these sites may increase, and the HELP and/or HEDE mechanism may become more dominant.

According to Neeraj et al. (2012) quasi-cleavage fracture occurs due to plasticity-generated and hydrogen-stabilized vacancy damage accumulation and nanovoid coalescence (i.e., HELP + HESIV) in ferritic steel. However, the nature of nanovoids in bcc metals may differ from that in fcc metals. Shimizu et al. (2020) previously studied the role of nanovoids in the hydrogen embrittlement of an Al–Zn–Mg–Cu alloy by high-resolution X-ray tomography in view of vacancy stabilization by hydrogen and three-dimensional nucleation, coalescence, and clustering of nanovoids. These authors indicated that most of the vacancies formed by deformation were not stabilized by hydrogen and did not grow into nanovoids because of the low occupation of hydrogen vacancies. Then, they concluded that the nanovoid contribution to HE fracture is minor. In the present case, the hydrogen occupancy of the vacancy was 2.9×10^{-3}, even at its maximum. Since this value is similar as reported their work (Shimizu et al., 2020), HESIV mechanism also did not appear to contribute to the HE in the Al-Zn-Mg alloy. Additionally, as mentioned above, because the contribution of the HELP mechanism could also be minor in the Al-Zn-Mg alloy, we concluded that the contribution of the HELP + HESIV model to HE fracture was also minor.

In Al-Zn-Mg alloys, the possibility of contributing the HEDE+HELP model to HE behavior was proposed (Bal et al., 2020; Moshtaghi et al., 2021). The authors discussed the contribution of each mechanism from the results of fracture surface observations (e.g., the presence of nanovoids on quasi-cleavage fracture surfaces). There was no quantitative discussion of the involvement of trapping sites for HE in terms of partitioned hydrogen concentration by Bal et al. (2020). Moshtaghi et al. (2021) evaluated the hydrogen concentration trapped at the lattice, dislocation, and grain boundary by analyzing hydrogen desorption peaks. However, it is misleading to assume that hydrogen was trapped only in lattice defects, ignoring the presence of precipitates, intermetallic compound particles, and other structures that can be strong trapping sites in multi-metallic alloys. In other words, as they also mentioned, it is highly likely that

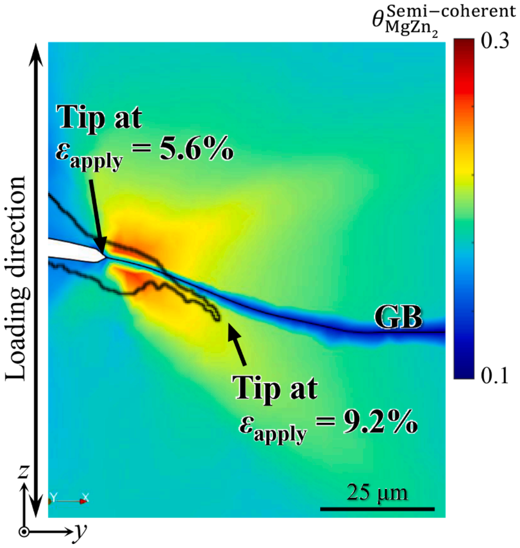

Fig. 11. The distribution of hydrogen occupancy of the semi-coherent interface of the $MgZn_2$ precipitate around the intergranular crack tip at $\varepsilon_{apply} = 5.6$ %. The cracks are superimposed on a cross-sectional image of the crack shape for which $\varepsilon_{apply} = 9.2$ %.

there are multiple peaks in the close temperature range, each overlapping each other and appearing as one peak. In other words, we recognize that no quantitative discussion has been made thus far on whether the hydrogen concentration is trapped enough to affect destruction. Based on this study, we expect that the contributions of these mechanisms to macroscopic fracture are still minor since, as already mentioned, the hydrogen concentrations trapped in dislocations, interstitials, and grain boundaries are limited and insufficient to cause the HELP + HEDE model.

Hydrogen partitioning analysis indicated that most of the hydrogen was partitioned to the $MgZn_2$ precipitates. In addition, Tsuru et al. (2020) reported that there were traces of $MgZn_2$ precipitate debonding on the quasi-cleavage fracture surface in an Al-Zn-Mg ternary alloy, and it is highly possible that the quasi-cleavage fracture was also caused by precipitate debonding in the present study. Therefore, the influence of the hydrogen partitioning behavior of the $MgZn_2$ precipitates on quasi-cleavage fracture was analyzed in detail. The distribution of hydrogen occupancy of the semi-coherent interface of the $MgZn_2$ precipitate is shown in Fig. 11. The occupancy reached its highest value ($\theta_{\mathrm{MgZn_2}}^{\mathrm{Semi-coherent}} = 0.28$), approximately 1.6 times the initial occupancy (i.e., to 0.18) in the vicinity of the crack tip, but did not reach the critical value for precipitate debonding. This means that the precipitate interface is prone to debonding due to hydrogen enrichment, suggesting that addition of other external factors causes precipitate interface debonding. To evaluate the transition behavior from intergranular cracks to quasi-cleavage cracks, the local hydrogen partitioning behavior ahead of the crack tip was evaluated. Fig. 12 shows the influence of hydrogen at the crack tip on the crack transition behavior. The horizontal axis is the distance from left to right of the specimen width (Fig. 3). Depending on the element size ahead of the crack tip, the stress and hydrogen concentration at the crack tip vary due to the sharp shape of the crack in the present FEM model. Note that the hydrogen occupancies at the crack tip shown in Fig. 12 are qualitative. Fig. 12 (a) shows that the quasi-cleavage cracks tended to initiate in the region where the hydrogen occupancy of the precipitate interface was slightly high (especially in the QCF region on the right side), but, this trend was not a clarity. Fig. 11 shows that the quasi-cleavage crack propagated toward the direction of the extended region of slightly high hydrogen occupancy. The quasi-cleavage crack may propagate in the direction of that the region where nano-cracks were generated by interfacial debonding of the precipitates was expanded. Therefore, it is possible that crack initiation was promoted by not only hydrogen occupancy at the crack tip but also that conditions in the appropriate range from the crack tip reach a condition for crack propagation (Hill and Panontin, 2002; Pluvinage and Capelle, 2014). Later, we will discuss the influence of hydrogen distribution rather than only hydrogen occupancy at the crack tip on the crack propagation process.

We examined the relationship between crack propagation and debonding behavior of the precipitate interface based on the distribution of the interfacial cohesive energy of the semi-coherent interface of the precipitate. The interfacial cohesive energy is the difference between the interface energies before and after the hydrogen configuration, and this energy indicates the strength of the atomic bonds at the interface as the minimum energy required for interfacial debonding. Shimizu et al. (2024) clarified the relationship between the number of hydrogen atoms trapped at the semi-coherent interface and the interfacial cohesive energy of the precipitate using first-principles calculations. Fig. 13 shows the distribution of the interfacial cohesive energy of the semi-coherent interface, calculated using the abovementioned relationship reported by Shimizu et al. (2024), and the distribution of hydrogen occupancy at the semi-coherent interface of the precipitate is shown in Fig. 11. The interfacial cohesive energy in the grain in which quasi-cleavage cracks propagated was 0.76 at the minimum (at location A in Fig. 13), and its value at the crack tip after propagation (location C in Fig. 13) was 0.82. According to Bhuiyan et al. (2016) the hydrogen concentration in an Al-Zn-Mg alloy not charged with hydrogen is approximately 2.29×10^{23} atoms H/m^3 (0.140 mass ppm), and the amount of hydrogen trapped at the semi-coherent interface of the precipitate, also in the absence of hydrogen charging, was 2.28×10^{23} atoms H/m^3 (0.139 mass ppm) according to the present hydrogen partitioning analysis. The interfacial cohesive energy was reduced to 0.89 from 1.05 (i.e., by approximately 15 %) solely due

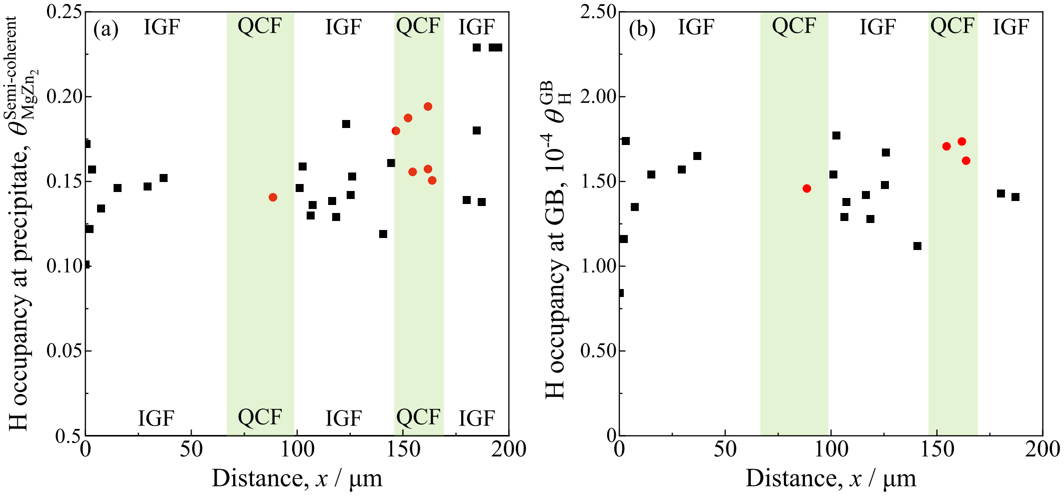

Fig. 12. Variation in the hydrogen occupancy of (a) the semi-coherent interface of precipitate and (b) the grain boundary ahead of the intergranular crack tip after 10 min of applied stress. The region in which the intergranular crack transitioned to a quasi-cleavage crack is indicated in green in both figures. The red points were obtained from elements through which the quasi-cleavage crack passed.

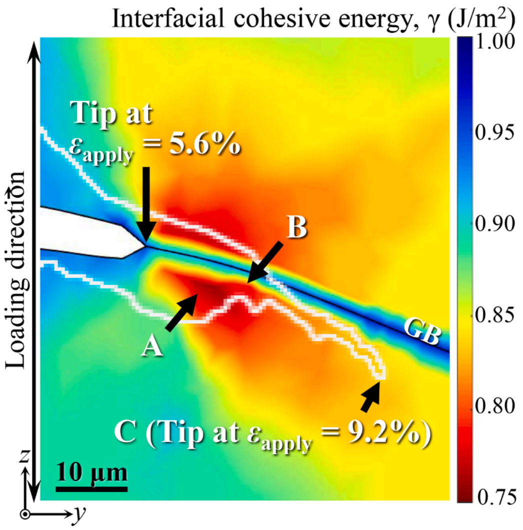

Fig. 13. The distribution of the interfacial cohesive energy of the semi-coherent interface of the $MgZn_2$ precipitates around the crack tip. The crack for which $\varepsilon_{apply} = 9.2$ % is superimposed in white.

to hydrogen charging by the EDM used in the present study. Due to the local hydrogen accumulation caused by stress concentration at the crack tip, the interfacial cohesive energy in the crack-propagated grain was up to 11 % lower than that in the unloaded state (and 25 % lower than that before hydrogen charging). Stress concentrations at the crack tip appear to result in higher stress perpendicular to the precipitate interface. The combination of reduced interfacial cohesive energy due to hydrogen charging and local hydrogen accumulation and the high normal stress acting on the interface of the precipitate ahead of the crack tip appears to lead to precipitate interface debonding, which in turn accelerates crack propagation.

The relationship between the crack propagation and debonding behavior of the $MgZn_2$ precipitate interface was investigated. Fig. 14 shows the variation in the increment of crack growth, Δa, which is the increase in the crack length due to increasing the applied strain from 5.6 % to 9.2 %. Fig. 15 shows the influence of the increase in the normal stress on the crack propagation increment and the hydrogen occupancy of the semi-coherent interface of the $MgZn_2$ precipitate. Note that Fig. 15 shows a qualitative relationship. No clear correlation was detected among the normal stress, hydrogen occupancy, or crack propagation increment behavior. In other words, the local hydrogen concentration and normal stress within a range of a few micrometers from the crack tip may not affect the increase in crack propagation over tens of micrometers. In addition, the hydrogen occupancy was not high in the entire region through which the crack propagated; the hydrogen occupancy at the crack tip after loading (location C in Fig. 13) was 0.22. This occupancy was only 1.2 times the initial state (i.e., 0.18). The interfacial cohesive energy reduction rate at location C was only 7 % compared to that in the unloaded state. This reduction ratio suggests that the cracks do not suddenly or rapidly propagate through the region where hydrogen accumulates. In other words, the crack propagation behavior was dependent not only on the stress and hydrogen concentration distributions while an applied strain was held but also on the continuous changes in these values at the crack tip during crack propagation. The crack shape at an applied strain of 9.2 % suggested that the crack may have blunted at location B in Fig. 13 and then propagated again as a quasi-cleavage crack. Since the increase in the crack length (16–58 μm) was greater than the increase in the hydrogen diffusion distance during loading (9.3 μm), the hydrogen concentration at the crack tip during propagation gradually decreased due to an insufficient hydrogen supply. As a result, the hydrogen concentration might fall below the minimum needed to promote interface debonding and crack propagation, so the cracks were temporarily blunted. Hydrogen was then supplied to the crack tip while in the blunted state, and the crack propagated again when the hydrogen concentration reached the critical hydrogen concentration for hydrogen-induced debonding of the precipitate. The hydrogen supply source could be not only internal hydrogen diffusion to the crack tip but also external hydrogen generated by the reaction between the fresh aluminum surface formed during crack propagation and water vapor in the atmosphere.

Finally, we summarize the quasi-cleavage crack propagation process. First, crack propagation starts due to the debonding behavior of the precipitate interface, especially in the region where the interfacial cohesive energy is significantly lower at the crack tip, such as at location A in Fig. 13. Since crack propagation proceeds faster than hydrogen diffusion, the continuous decrease in hydrogen concentration ahead of the crack tip during propagation leads to the criterion for interface debonding, and associated crack propagation criteria are no longer met, resulting in crack blunting. The crack then propagates again when the hydrogen concentration ahead of the crack tip reaches the level at which debonding of the precipitate can take place. Based on the above, we conclude that dynamic hydrogen partitioning to the precipitate interface may contribute to crack initiation and propagation. The evidence shows that HE behavior can be suppressed by reducing hydrogen trapping at the $MgZn_2$ precipitate interface by increasing the number of IMC particles that have higher hydrogen trap energies than that of the precipitate interface (Safyari et al., 2021; Su et al., 2019; Yamaguchi et al., 2020). In future work, the multi-dimensional relationships among the local stress acting on the precipitate interface, the local hydrogen concentration, and fracture will be clarified by evaluating the HE behavior via reasonable experiments and simulations.

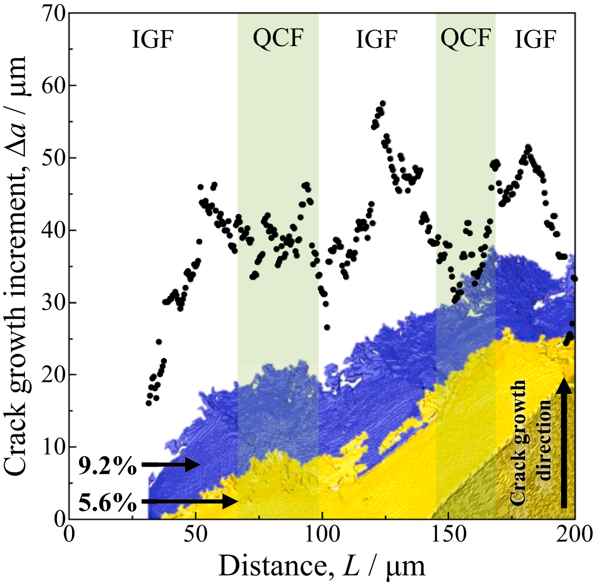

Fig. 14. Variation in the crack growth increment, Δa, from $\varepsilon_{\text{apply}} = 5.6$ % to 9.2 %. The cracks are superimposed in yellow ($\varepsilon_{\text{apply}} = 5.6$ %) and blue ($\varepsilon_{\text{apply}} = 9.2$ %). The regions where the intergranular crack transitioned to the quasi-cleavage crack are shown in green.

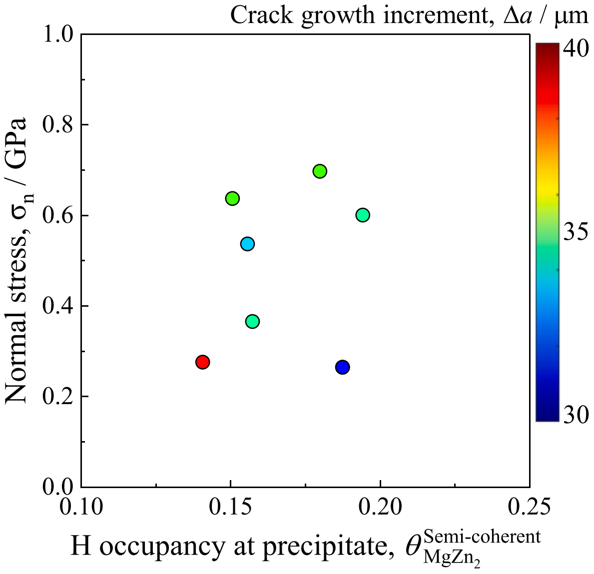

Fig. 15. The relationship among the crack growth behavior, normal stress against the crack growth direction, and hydrogen occupancy of the semi-coherent interface of the $MgZn_2$ precipitate at the crack tip. The colors correspond to the crack growth increment values on the color map.

As shown in Fig. 12 (a), there were regions where cracks propagated as intergranular cracks, even when the hydrogen occupancy of the precipitate interface was high. The present analysis did not clarify this phenomenon. Yamaguchi et al. (2019) and Liang et al. (2021) revealed that hydrogen accumulation on grain boundaries leads to a reduction in the interfacial cohesive energy of grain boundaries. In addition, Yamaguchi et al. (2019) revealed that grain boundaries debond when the amount of hydrogen at the boundaries reaches a critical hydrogen concentration for hydrogen-induced debonding of the grain boundary. Even the maximum value of the hydrogen occupancy of the grain boundary, as shown in Fig. 12 (b), was 1000 times lower than the critical hydrogen concentration. Intergranular crack propagation is not dominated by hydrogen alone. Toda et al. (2023) applied a microstructural optimization method with metamodeling to investigate the correlation between the polycrystalline microstructure of an Al-Zn-Mg alloy and its HE behavior. They proposed that the weakest grain boundaries against HE are those with a smaller grain boundary area, grain boundaries oriented perpendicular to the loading direction, and grain volumes relatively closely surrounding a grain boundary triple junction. However, the correlation coefficients of these factors for fractures were significantly low. Factors other than crystallographic factors, which were not considered in their study, could be dominant for HE. As other possible dominant factors, solid solution elements and precipitates on the grain boundaries could affect the intergranular crack propagation behavior. First, the effect of solid solution elements was considered. Ohte et al. (2019) reported, via numerical simulations, that Zn and Mg act as grain boundary embrittlement elements. However, these elements cannot segregate on grain boundaries due to their positive grain boundary segregation energies (Ohte et al., 2019), which has been experimentally confirmed (Kairy et al., 2018). Thus, solid solution elements were not considered to have influenced the intergranular cracking in the present study. Second, the effect of grain boundary precipitates (GBPs) was considered. GBPs exhibit an incoherent interface with the aluminum matrix (Vasudévan and Doherty, 1987; Viswanadham et al., 1980). According to a recent report by Yamaguchi et al. (2023), the interfacial cohesive energy of the incoherent interface of IMC particles decreases with increasing hydrogen concentration. However, hydrogen-induced spontaneous debonding does not occur at the incoherent interface (Yamaguchi et al., 2023). This report suggested that interfacial debonding at the incoherent interface of GBPs might occur for reasons other than hydrogen accumulation only. The combination of reduced interfacial cohesive energy due to hydrogen accumulation and the stress concentration around the grain boundaries might enhance the interfacial debonding of GBPs, and this debonding behavior could lead to intergranular crack propagation.

6. Conclusion

The present study is the first image-based analysis of the relationship between hydrogen accumulation behavior and macroscopic hydrogen embrittlement fracture behavior. To simulate local hydrogen accumulation and hydrogen partitioning behavior, an unprecedented multi-modal 3D image-based simulation combining the CPFEM and hydrogen diffusion analysis at the mesoscale was established. This has allowed to directly correlate the actual fracture behavior with the mechanical response and hydrogen accumulation behavior. In addition, detailed analysis, especially in the hydrogen embrittlement region, has enabled the evaluation of the influence of local hydrogen accumulation behavior and the associated dynamic hydrogen distribution behavior on the actual hydrogen embrittlement behavior.

The stress and strain distributions were affected not only by the deformation behavior of individual grains but also by the interactions among neighboring grains. A case in which the plastic strain was localized in grains with higher (rather than lower) deformation resistance was discovered. The maximum hydrostatic stress increased to more than 1.25 GPa in the vicinity of the intergranular crack tip due to a deformation mismatch among neighboring grains. The increase in the hydrogen concentration was more pronounced in the vicinity of the crack tip, reaching 1.75 times the initial concentration in this vicinity after 10 min of applied stress.

The hydrogen partitioning behavior caused by hydrogen accumulation under stress was also evaluated. The accumulated hydrogen was mainly repartitioned to the vacancies and precipitate interfaces near the crack tips. The hydrogen occupancy of the semi-coherent interface of the precipitate increased locally in the vicinity of the crack tip and reached 0.28.

The quasi-cleavage crack propagated in the region where the interfacial cohesive energy of the semi-coherent interface of the $MgZn_2$ precipitate was reduced by hydrogen accumulation near the crack tip. This result agrees with the recently proposed mechanism in which the nanoscopic hydrogen-induced debonding behavior of the $MgZn_2$ precipitate interface causes quasi-cleavage fracturing. Hydrogen embrittlement in the Al-Zn-Mg alloy was dominated by dynamic hydrogen partitioning to the $MgZn_2$ precipitate interface.

In future work, the multi-dimensional relationships among the local stress acting on the precipitate interface, the local hydrogen concentration, and the fracture process will be clarified by evaluating the hydrogen embrittlement behavior via reasonable experiments and simulations.

CRediT authorship contribution statement

Hiro Fujihara: Writing – original draft, Visualization, Software, Methodology, Investigation, Funding acquisition, Formal analysis, Data curation, Conceptualization. **Hiroyuki Toda:** Writing – review & editing, Supervision, Resources, Project administration, Funding acquisition, Conceptualization. **Ken-ichi Ebihara:** Writing – review & editing, Software, Resources, Methodology. **Masakazu Kobayashi:** Writing – review & editing, Software, Resources, Methodology, Investigation. **Tsuyoshi Mayama:** Writing – review & editing, Visualization, Software, Methodology, Investigation. **Kyosuke Hirayama:** Writing – review & editing, Software, Methodology, Investigation. **Kazuyuki Shimizu:** Writing – review & editing, Software, Methodology, Investigation. **Akihisa Takeuchi:** Writing – review & editing, Software, Resources, Investigation. **Masayuki Uesugi:** Writing – review & editing, Software, Resources, Investigation.

Declaration of competing interest

The authors declare that they have no known competing financial interests or personal relationships that could have appeared to influence the work reported in this paper.

Data availability

Data will be made available on request.

Acknowledgments

This study was supported by the Japan Science and Technology Agency (JST) under Collaborative Research Based on Industrial Demand “Heterogeneous Structure Control: Toward Innovative Development of Metallic Structural Materials”, Grant No. JPMJSK1412, Japan and JST CREST Grant No. JPMJCR1995, Japan. The synchrotron radiation experiments were performed at the BL20XU of SPring-8 with the approval of the Japan Synchrotron Radiation Research Institute (JASRI) (Proposal No. 2018A0076). The study was also supported by JSPS KAKENHI Grant No’s. JP20J11740 and JP23K13564. It was also supported in part by a grant from the Light Metal Educational Foundation, Japan. The authors also thank Mr. Shogo Yasuda for contributing to the crystal plasticity finite element analysis.

References

Asaro, R.J., Rice, J.R., 1977. Strain localization in ductile single crystals. J. Mech. Phys. Solids 25, 309–338. https://doi.org/10.1016/0022-5096(77)90001-1.

Ashby, M.F., 1970. The deformation of plastically non-homogeneous materials. Philos. Mag. A J. Theor. Exp. Appl. Phys. 21, 399–424. https://doi.org/10.1080/14786437008238426.

Bal, B., Okdem, B., Bayram, F.C., Aydin, M., 2020. A detailed investigation of the effect of hydrogen on the mechanical response and microstructure of Al 7075 alloy under medium strain rate impact loading. Int. J. Hydrogen Energy 45, 25509–25522. https://doi.org/10.1016/j.ijhydene.2020.06.241.

Barrera, O., Tarleton, E., Tang, H.W., Cocks, A.C.F., 2016. Modelling the coupling between hydrogen diffusion and the mechanical behaviour of metals. Comput. Mater. Sci. 122, 219–228. https://doi.org/10.1016/j.commatsci.2016.05.030.

Bendo, A., Matsuda, K., Lee, S., Nishimura, K., Nunomura, N., Toda, H., Yamaguchi, M., Tsuru, T., Hirayama, K., Shimizu, K., Gao, H., Ebihara, K., Itakura, M., Yoshida, T., Murakami, S., 2018a. Atomic scale HAADF-STEM study of η' and η_1 phases in peak-aged Al–Zn–Mg alloys. J. Mater. Sci. 53, 4598–4611. https://doi.org/10.1007/s10853-017-1873-0.

Bendo, A., Matsuda, K., Lee, S., Nishimura, K., Toda, H., Shimizu, K., Tsuru, T., Yamaguchi, M., 2018b. Microstructure evolution in a hydrogen charged and aged Al–Zn–Mg alloy. Materialia 3, 50–56. https://doi.org/10.1016/j.mtla.2018.09.035.

Bhuiyan, M.S., Tada, Y., Toda, H., Hang, S., Uesugi, K., Takeuchi, A., Sakaguchi, N., Watanabe, Y., 2016. Influences of hydrogen on deformation and fracture behaviors of high Zn 7XXX aluminum alloys. Int. J. Fract. 200, 13–29. https://doi.org/10.1007/s10704-016-0092-z.

Birnbaum, H.K., Sofronis, P., 1994. Hydrogen-enhanced localized plasticity—a mechanism for hydrogen-related fracture. Mater. Sci. Eng. A 176, 191–202. https://doi.org/10.1016/0921-5093(94)90975-X.

Brinckmann, S., Siegmund, T., Huang, Y., 2006. A dislocation density based strain gradient model. Int. J. Plast. 22, 1784–1797. https://doi.org/10.1016/j.ijplas.2006.01.005.

Carling, K., Wahnström, G., Mattsson, T.R., Mattsson, A.E., Sandberg, N., Grimvall, G., 2000. Vacancies in metals: from first-principles calculations to experimental data. Phys. Rev. Lett. 85, 3862–3865. https://doi.org/10.1103/PhysRevLett.85.3862.

Dadfarnia, M., Martin, M.L., Nagao, A., Sofronis, P., Robertson, I.M., 2015. Modeling hydrogen transport by dislocations. J. Mech. Phys. Solids 78, 511–525. https://doi.org/10.1016/j.jmps.2015.03.002.

Deng, Y., Barnoush, A., 2018. Hydrogen embrittlement revealed via novel *in situ* fracture experiments using notched micro-cantilever specimens. Acta Mater. 142, 236–247. https://doi.org/10.1016/j.actamat.2017.09.057.

Djukic, M.B., Bakic, G.M., Sijacki Zeravcic, V., Sedmak, A., Rajicic, B., 2019. The synergistic action and interplay of hydrogen embrittlement mechanisms in steels and iron: localized plasticity and decohesion. Eng. Fract. Mech. 216, 106528 https://doi.org/10.1016/j.engfracmech.2019.106528.

Djukic, M.B., Sijacki Zeravcic, V., Bakic, G.M., Sedmak, A., Rajicic, B., 2015. Hydrogen damage of steels: a case study and hydrogen embrittlement model. Eng. Fail. Anal. 58, 485–498. https://doi.org/10.1016/j.engfailanal.2015.05.017.

Ebihara, K., Itakura, M., Yamaguchi, M., Kaburaki, H., Suzudo, T., 2011. Evaluation of stress and hydrogen concentration at grain boundary of steels using three-dimensional polycrystalline model. Prog. Nucl. Sci. Technol. 2, 38–43. https://doi.org/10.15669/pnst.2.38.

Elkot, M.N., Sun, B., Zhou, X., Ponge, D., Raabe, D., 2022. Hydrogen-assisted decohesion associated with nanosized grain boundary κ-carbides in a high-Mn lightweight steel. Acta Mater. 241, 118392 https://doi.org/10.1016/j.actamat.2022.118392.

Enomoto, T., Matsumoto, R., Taketomi, S., Miyazaki, N., 2010. First-principles estimation of hydrogen occupancy around lattice defects in Al. J. Soc. Mater. Sci. Jpn. 59, 596–603. https://doi.org/10.2472/jsms.59.596.

Fernández-Sousa, R., Betegón, C., Martínez-Pañeda, E., 2022. Cohesive zone modelling of hydrogen assisted fatigue crack growth: the role of trapping. Int. J. Fatigue 162. https://doi.org/10.1016/j.ijfatigue.2022.106935.

Gao, P.F., Fei, M.Y., Zhan, M., Fu, M.W., 2023. Microstructure- and damage-nucleation-based crystal plasticity finite element modeling for the nucleation of multi-type voids during plastic deformation of Al alloys. Int. J. Plast. 165 https://doi.org/10.1016/j.ijplas.2023.103609.

Guo, Y., Collins, D.M., Tarleton, E., Hofmann, F., Tischler, J., Liu, W., Xu, R., Wilkinson, A.J., Britton, T.B., 2015. Measurements of stress fields near a grain boundary: exploring blocked arrays of dislocations in 3D. Acta Mater. 96, 229–236. https://doi.org/10.1016/j.actamat.2015.05.041.

Hayashi, Y., Setoyama, D., Hirose, Y., Yoshida, T., Kimura, H., 2019. Intragranular three-dimensional stress tensor fields in plastically deformed polycrystals. Science 366, 1492–1496. https://doi.org/10.1126/science.aax9167 (80-.).

Hill, M.R., Panontin, T.L., 2002. Micromechanical modeling of fracture initiation in 7050 aluminum. Eng. Fract. Mech. 69, 2163–2186. https://doi.org/10.1016/S0013-7944(01)00148-5.

Huang, Y., 1991. A User-Material Subroutine Incorporating Single Crystal Plasticity in the Abaqus Finite Element Program. Harvard University.

Huang, Y., Qu, S., Hwang, K.C., Li, M., Gao, H., 2004. A conventional theory of mechanism-based strain gradient plasticity. Int. J. Plast. 20, 753–782. https://doi.org/10.1016/j.ijplas.2003.08.002.

Isfandbod, M., Martínez-Pañeda, E., 2021. A mechanism-based multi-trap phase field model for hydrogen assisted fracture. Int. J. Plast. 144, 1–19. https://doi.org/10.1016/j.ijplas.2021.103044.

Ismer, L., Park, M.S., Janotti, A., Van de Walle, C.G., 2009. Interactions between hydrogen impurities and vacancies in Mg and Al: a comparative analysis based on density functional theory. Phys. Rev. B 80, 184110. https://doi.org/10.1103/PhysRevB.80.184110.

Hutchinson, J.W., 1976. Bounds and self-consistent estimates for creep of polycrystalline materials. Proc. R. Soc. Lond. A Math. Phys. Sci. 348, 101–127. https://doi.org/10.1098/rspa.1976.0027.

Jiang, M., Fan, Z., Kruch, S., Devincre, B., 2022. Grain size effect of FCC polycrystal: a new CPFEM approach based on surface geometrically necessary dislocations. Int. J. Plast. 150 https://doi.org/10.1016/j.ijplas.2021.103181.

Kairy, S.K., Turk, S., Birbilis, N., Shekhter, A., 2018. The role of microstructure and microchemistry on intergranular corrosion of aluminium alloy AA7085-T7452. Corros. Sci. 143, 414–427. https://doi.org/10.1016/j.corsci.2018.08.033.

Khan, A.S., Liu, J., Yoon, J.W., Nambori, R., 2015. Strain rate effect of high purity aluminum single crystals: experiments and simulations. Int. J. Plast. 67, 39–52. https://doi.org/10.1016/j.ijplas.2014.10.002.

Khoei, A.R., Yasbolaghi, R., Biabanaki, S.O.R., 2015. A polygonal finite element method for modeling crack propagation with minimum remeshing. Int. J. Fract. 194, 123–148. https://doi.org/10.1007/s10704-015-0044-z.

Kobayashi, M., Matsuyama, T., Kouno, A., Toda, H., Miura, H., 2016. Construction of finite element meshes for polycrystal grains model from X-ray CT image. Mater. Trans. 57, 2089–2096. https://doi.org/10.2320/matertrans.M2016260.

Krom, A.H.M., Koers, R.W.J., Bakker, A., 1999. Hydrogen transport near a blunting crack tip. J. Mech. Phys. Solids 47, 971–992. https://doi.org/10.1016/S0022-5096(98)00064-7.

Kröner, E., 1959. Allgemeine kontinuumstheorie der versetzungen und eigenspannungen. Arch. Ration. Mech. Anal. 4, 273–334. https://doi.org/10.1007/BF00281393.

Lee, E.H., Liu, D.T., 1967. Finite-strain elastic—plastic theory with application to plane-wave analysis. J. Appl. Phys. 38, 19–27. https://doi.org/10.1063/1.1708953.

Li, J.C.M., Oriani, R.A., Darken, L.S., 1966. The thermodynamics of stressed solids. Z. Phys. Chem. 49, 271–290. https://doi.org/10.1524/zpch.1966.49.3_5.271.

Liang, S., Huang, M., Zhao, L., Zhu, Y., Li, Z., 2021. Effect of multiple hydrogen embrittlement mechanisms on crack propagation behavior of FCC metals: competition vs. synergy. Int. J. Plast. 143, 103023 https://doi.org/10.1016/j.ijplas.2021.103023.

Liu, Y., Adande, S., Britton, T.B., Dunne, F.P.E., 2021. Cold dwell fatigue analyses integrating crystal-level strain rate sensitivity and microstructural heterogeneity. Int. J. Fatigue 151. https://doi.org/10.1016/j.ijfatigue.2021.106398.

Liu, Y., Dunne, F.P.E., 2021. The mechanistic link between macrozones and dwell fatigue in titanium alloys. Int. J. Fatigue 142, 105971. https://doi.org/10.1016/j.ijfatigue.2020.105971.

Lorensen, W.E., Cline, H.E., 1987. Marching cubes: a high resolution 3D surface construction algorithm. ACM SIGGRAPH Comput. Graph. 21, 163–169. https://doi.org/10.1145/37402.37422.

Ludwig, W., King, A., Reischig, P., Herbig, M., Lauridsen, E.M., Schmidt, S., Proudhon, H., Forest, S., Cloetens, P., Roscoat, S.R.du, Buffière, J.Y., Marrow, T.J., Poulsen, H.F., 2009. New opportunities for 3D materials science of polycrystalline materials at the micrometre lengthscale by combined use of X-ray diffraction and X-ray imaging. Mater. Sci. Eng. A 524, 69–76. https://doi.org/10.1016/j.msea.2009.04.009.

Lynch, S., 2012. Hydrogen embrittlement phenomena and mechanisms. Corros. Rev. 30, 105–123. https://doi.org/10.1515/corrrev-2012-0502.

Martínez-Pañeda, E., Del Busto, S., Niordson, C.F., Betegón, C., 2016. Strain gradient plasticity modeling of hydrogen diffusion to the crack tip. Int. J. Hydrog. Energy 41, 10265–10274. https://doi.org/10.1016/j.ijhydene.2016.05.014.

Mayama, T., Ohashi, T., Kondou, R., 2009. Geometrically necessary dislocation structure organization in FCC bicrystal subjected to cyclic plasticity. Int. J. Plast. 25, 2122–2140. https://doi.org/10.1016/j.ijplas.2009.02.001.

Militzer, M., Sun, W.P., Jonas, J.J., 1994. Modelling the effect of deformation-induced vacancies on segregation and precipitation. Acta Metall. Mater. 42, 133–141. https://doi.org/10.1016/0956-7151(94)90056-6.

Miresmaeili, R., Saintier, N., Notsu, H., Olive, J.-M., Kanayama, H., 2010. One-way coupled crystal plasticity-hydrogen diffusion simulation on artificial microstructure. J. Comput. Sci. Technol. 4, 105–120. https://doi.org/10.1299/jcst.4.105.

Moshtaghi, M., Safyari, M., Kuramoto, S., Hojo, T., 2021. Unraveling the effect of dislocations and deformation-induced boundaries on environmental hydrogen embrittlement behavior of a cold-rolled Al–Zn–Mg–Cu alloy. Int. J. Hydrog. Energy 46, 8285–8299. https://doi.org/10.1016/j.ijhydene.2020.12.028.

Nagumo, M., 2004. Hydrogen related failure of steels – a new aspect. Mater. Sci. Technol. 20, 940–950. https://doi.org/10.1179/026708304225019687.

Nagumo, M., Takai, K., 2019. The predominant role of strain-induced vacancies in hydrogen embrittlement of steels: overview. Acta Mater. 165, 722–733. https://doi.org/10.1016/j.actamat.2018.12.013.

Neeraj, T., Srinivasan, R., Li, J., 2012. Hydrogen embrittlement of ferritic steels: observations on deformation microstructure, nanoscale dimples and failure by nanovoiding. Acta Mater. 60, 5160–5171. https://doi.org/10.1016/j.actamat.2012.06.014.

Nye, J.F., 1953. Some geometrical relations in dislocated crystals. Acta Metall. 1, 153–162. https://doi.org/10.1016/0001-6160(53)90054-6.

Ohashi, T., Kawamukai, M., Zbib, H., 2007. A multiscale approach for modeling scale-dependent yield stress in polycrystalline metals. Int. J. Plast. 23, 897–914. https://doi.org/10.1016/j.ijplas.2006.10.002.

Ohte, R., Yamada, T., Uesugi, T., Takigawa, Y., Higashi, K., 2019. Effect of a small amount of Fe-addition on intergranular fracture of Al–7.3 mass%Mg alloys. J. Jpn. Inst. Light Met. 69, 457–464. https://doi.org/10.2464/jilm.69.457.

Oriani, R., 1970. The diffusion and trapping of hydrogen in steel. Acta Metall. 18, 147–157. https://doi.org/10.1016/0001-6160(70)90078-7.

Oriani, R.A., Josephic, P.H., 1974. Equilibrium aspects of hydrogen-induced cracking of steels. Acta Metall. 22, 1065–1074. https://doi.org/10.1016/0001-6160(74)90061-3.

Pan, J., Rice, J.R., 1983. Rate sensitivity of plastic flow and implications for yield-surface vertices. Int. J. Solids Struct. 19, 973–987. https://doi.org/10.1016/0020-7683(83)90023-9.

Peirce, D., Asaro, R.J., Needleman, A., 1983. Material rate dependence and localized deformation in crystalline solids. Acta Metall. 31, 1951–1976. https://doi.org/10.1016/0001-6160(83)90014-7.

Peirce, D., Asaro, R.J.J., Needleman, A., 1982. An analysis of nonuniform and localized deformation in ductile single crystals. Acta Metall. 30, 1087–1119. https://doi.org/10.1016/0001-6160(82)90005-0.

Pluvinage, G., Capelle, J., 2014. On characteristic lengths used in notch fracture mechanics. Int. J. Fract. 187, 187–197. https://doi.org/10.1007/s10704-013-9924-2.

Pouillier, E., Gourgues, A.F., Tanguy, D., Busso, E.P., 2012. A study of intergranular fracture in an aluminium alloy due to hydrogen embrittlement. Int. J. Plast. 34, 139–153. https://doi.org/10.1016/j.ijplas.2012.01.004.

Raabe, D., Roters, F., 2004. Using texture components in crystal plasticity finite element simulations. Int. J. Plast. 20, 339–361. https://doi.org/10.1016/S0749-6419(03)00092-5.

Robertson, I.M., Sofronis, P., Nagao, A., Martin, M.L., Wang, S., Gross, D.W., Nygren, K.E., 2015. Hydrogen embrittlement understood. Metall. Mater. Trans. A 46, 2323–2341. https://doi.org/10.1007/s11661-015-2836-1.

Safyari, M., Moshtaghi, M., Kuramoto, S., 2021. On the role of traps in the microstructural control of environmental hydrogen embrittlement of a 7xxx series aluminum alloy. J. Alloy. Compd. 855, 157300 https://doi.org/10.1016/j.jallcom.2020.157300.

Shimizu, K., Toda, H., Fujihara, H., Hirayama, K., Uesugi, K., Takeuchi, A., 2019. Hydrogen partitioning behavior and related hydrogen embrittlement in Al-Zn-Mg alloys. Eng. Fract. Mech. 216, 106503 https://doi.org/10.1016/j.engfracmech.2019.106503.

Shimizu, K., Toda, H., Hirayama, K., Fujihara, H., Tsuru, T., Yamaguchi, M., Bendo, A., Matsuda, K., Uesugi, M., Takeuchi, A., 2024. Hydrogen embrittlement in Al-Zn-Mg alloys: semi-spontaneous decohesion at precipitates. Acta Mater. to be submitted.

Shimizu, K., Toda, H., Kadogawa, C., Fujihara, H., Takeuchi, A., 2020. Influence of nanovoids in the hydrogen embrittlement fracture of Al–Zn–Mg–Cu alloys. Materialia 11, 100667. https://doi.org/10.1016/j.mtla.2020.100667.

Shimokawa, T., Nakatani, A., Kitagawa, H., 2005. Grain-size dependence of the relationship between intergranular and intragranular deformation of nanocrystalline Al by molecular dynamics simulations. Phys. Rev. B 71, 224110. https://doi.org/10.1103/PhysRevB.71.224110.

Singaravelu, A.S.S., Williams, J.J., Goyal, H.D., Niverty, S., Singh, S.S., Stannard, T.J., Xiao, X., Chawla, N., 2020. 3D time-resolved observations of fatigue crack initiation and growth from corrosion pits in Al 7XXX alloys using *in situ* synchrotron X-ray tomography. Metall. Mater. Trans. A Phys. Metall. Mater. Sci. 51, 28–41. https://doi.org/10.1007/s11661-019-05519-z.

Sofronis, P., McMeeking, R.M., 1989. Numerical analysis of hydrogen transport near a blunting crack tip. J. Mech. Phys. Solids 37, 317–350. https://doi.org/10.1016/0022-5096(89)90002-1.

Stannard, T.J., Williams, J.J., Singh, S.S., Sundaram Singaravelu, A.S., Xiao, X., Chawla, N., 2018. 3D time-resolved observations of corrosion and corrosion-fatigue crack initiation and growth in peak-aged Al 7075 using synchrotron X-ray tomography. Corros. Sci. 138, 340–352. https://doi.org/10.1016/j.corsci.2018.04.029.

Su, H., Toda, H., Masunaga, R., Shimizu, K., Gao, H., Sasaki, K., Bhuiyan, M.S., Uesugi, K., Takeuchi, A., Watanabe, Y., 2018. Influence of hydrogen on strain localization and fracture behavior in Al Zn Mg Cu aluminum alloys. Acta Mater. 159, 332–343. https://doi.org/10.1016/j.actamat.2018.08.024.

Su, H., Toda, H., Shimizu, K., Uesugi, K., Takeuchi, A., Watanabe, Y., 2019. Assessment of hydrogen embrittlement via image-based techniques in Al–Zn–Mg–Cu aluminum alloys. Acta Mater. 176, 96–108. https://doi.org/10.1016/j.actamat.2019.06.056.

Tabata, T., Birnbaum, H.K., 1984. Direct observations of hydrogen enhanced crack propagation in iron. Scr. Metall. 13, 576. https://doi.org/10.1016/0036-9748(84)90513-1.

Tabata, T., Birnbaum, H.K., 1983. Direct observations of the effect of hydrogen on the behavior of dislocations in iron. Scr. Metall. 17, 947–950. https://doi.org/10.1016/0036-9748(83)90268-5.

Takai, K., Shoda, H., Suzuki, H., Nagumo, M., 2008. Lattice defects dominating hydrogen-related failure of metals. Acta Mater. 56, 5158–5167. https://doi.org/10.1016/j.actamat.2008.06.031.

Toda, H., Hirayama, K., Yamaguchi, S., Fujihara, H., Higa, R., Shimizu, K., Takeuchi, A., Uesugi, M., 2023. Dominant factors controlling the initiation of hydrogen embrittlement in Al-Zn-Mg alloy. Mater. Trans. https://doi.org/10.2320/matertrans.MT-M2023116. MT-M2023116.

Toda, H., Kamiko, T., Tanabe, Y., Kobayashi, M., Leclere, D.J., Uesugi, K., Takeuchi, A., Hirayama, K., 2016. Diffraction-amalgamated grain boundary tracking for mapping 3D crystallographic orientation and strain fields during plastic deformation. Acta Mater. 107, 310–324. https://doi.org/10.1016/j.actamat.2016.01.072.

Tondro, A., Abdolvand, H., 2022. On the effects of texture and microstructure on hydrogen transport towards notch tips: a CPFE study. Int. J. Plast. 152, 103234 https://doi.org/10.1016/j.ijplas.2022.103234.

Troiano, A.R., 2016. The role of hydrogen and other interstitials in the mechanical behavior of metals. Metallogr. Microstruct. Anal. 5, 557–569. https://doi.org/10.1007/s13632-016-0319-4.

Tsuru, T., Shimizu, K., Yamaguchi, M., Itakura, M., Ebihara, K., Bendo, A., Matsuda, K., Toda, H., 2020. Hydrogen-accelerated spontaneous microcracking in high-strength aluminium alloys. Sci. Rep. 10, 1998. https://doi.org/10.1038/s41598-020-58834-6.

Tsuru, T., Yamaguchi, M., Ebihara, K., Itakura, M., Shiihara, Y., Matsuda, K., Toda, H., 2018. First-principles study of hydrogen segregation at the $MgZn_2$ precipitate in Al-Mg-Zn alloys. Comput. Mater. Sci. 148, 301–306. https://doi.org/10.1016/j.commatsci.2018.03.009.

Vasudévan, A.K., Doherty, R.D., 1987. Grain boundary ductile fracture in precipitation hardened aluminum alloys. Acta Metall. 35, 1193–1219. https://doi.org/10.1016/0001-6160(87)90001-0.

Viswanadham, R.K., Sun, T.S., Green, J.A.S., 1980. Grain boundary segregation in Al-Zn-Mg alloys-implications to stress corrosion cracking. Metall. Mater. Trans. A 11, 85–89. https://doi.org/10.1007/BF02700441.

Wang, Y., Toda, H., Xu, Y., Shimizu, K., Hirayama, K., Fujihara, H., Takeuchi, A., Uesugi, M., 2022. *In-situ* 3D observation of hydrogen-assisted particle damage behavior in 7075 Al alloy by synchrotron X-ray tomography. Acta Mater. 227, 117658 https://doi.org/10.1016/j.actamat.2022.117658.

Wasim, M., Djukic, M.B., Ngo, T.D., 2021. Influence of hydrogen-enhanced plasticity and decohesion mechanisms of hydrogen embrittlement on the fracture resistance of steel. Eng. Fail. Anal. 123, 105312 https://doi.org/10.1016/j.engfailanal.2021.105312.

Xie, D., Li, S., Li, M., Wang, Z., Gumbsch, P., Sun, J., Ma, E., Li, J., Shan, Z., 2016. Hydrogenated vacancies lock dislocations in aluminium. Nat. Commun. 7, 1–7. https://doi.org/10.1038/ncomms13341.

Yamaguchi, M., Ebihara, K., Itakura, M., Tsuru, T., Matsuda, K., Toda, H., 2019. First-principles calculation of multiple hydrogen segregation along aluminum grain boundaries. Comput. Mater. Sci. 156, 368–375. https://doi.org/10.1016/j.commatsci.2018.10.015.

Yamaguchi, M., Ebihara, K., Tsuru, T., Itakura, M., 2023. First-principles calculations of hydrogen trapping energy on incoherent interfaces of aluminum alloys. Mater. Trans. MT–M2023106. https://doi.org/10.2320/matertrans.MT-M2023106.

Yamaguchi, M., Itakura, M., Tsuru, T., Ebihara, K., 2021. Hydrogen-trapping energy in screw and edge dislocations in aluminum: first-principles calculations. Mater. Trans. 62, 582–589. https://doi.org/10.2320/matertrans.MT-M2020375.

Yamaguchi, M., Tsuru, T., Ebihara, K., Itakura, M., 2018. Surface energy reduction by dissociative hydrogen adsorption on inner surface of pore in aluminum. J. Jpn. Inst. Light Met. 68, 588–595. https://doi.org/10.2464/jilm.68.588.

Yamaguchi, M., Tsuru, T., Ebihara, K., Itakura, M., Matsuda, K., Shimizu, K., Toda, H., 2020. Hydrogen trapping in Mg_2Si and Al_7FeCu_2 intermetallic compounds in aluminum alloy: first-principles calculations. Mater. Trans. 61, 1907–1911. https://doi.org/10.2320/matertrans.MT-M2020201.

Young, G.A., Scully, J.R., 2002. The effects of test temperature, temper, and alloyed copper on the hydrogen-controlled crack growth rate of an Al-Zn-Mg-(Cu) alloy. Metall. Mater. Trans. A 33, 1167–1181. https://doi.org/10.1007/s11661-002-0218-y.

Yuan, S., Zhu, Y., Huang, M., Liang, S., Li, Z., 2020. Dislocation-density based crystal plasticity model with hydrogen-enhanced localized plasticity in polycrystalline face-centered cubic metals. Mech. Mater. 148, 103472 https://doi.org/10.1016/j.mechmat.2020.103472.

Yuan, S., Zhu, Y., Huang, M., Zhao, L., Liang, S., Li, Z., 2023. A coupled diffusional-mechanical model accounting for hydrogen enhancements of strain-induced dislocations and vacancies. Mech. Mater. 186, 104781 https://doi.org/10.1016/j.mechmat.2023.104781.

Zhao, Y., Niverty, S., Ma, X., Liu, X., Chawla, N., 2020. 3D grain structure of an extruded 6061 Al alloy by lab-scale X-ray diffraction contrast tomography (DCT). Mater. Charact. 170, 110716 https://doi.org/10.1016/j.matchar.2020.110716.

Zhou, Y., Neale, K.W., Tóth, L.S., 1993. A modified model for simulating latent hardening during the plastic deformation of rate-dependent FCC polycrystals. Int. J. Plast. 9, 961–978. https://doi.org/10.1016/0749-6419(93)90061-T.

Zhu, Y., Li, Z., Huang, M., Fan, H., 2017. Study on interactions of an edge dislocation with vacancy-H complex by atomistic modelling. Int. J. Plast. 92, 31–44. https://doi.org/10.1016/j.ijplas.2017.03.003.